ΕΘΝΙΚΟ ΜΕΤΣΟΒΙΟ ΠΟΛΥΤΕΧΝΕΙΟ
ΣΧΟΛΗ ΕΦΑΡΜΟΣΜΕΝΩΝ ΜΑΘΗΜΑΤΙΚΩΝ ΚΑΙ ΦΥΣΙΚΩΝ ΕΠΙΣΤΗΜΩΝ

ΤΟΜΕΑΣ ΦΥΣΙΚΗΣ
ΕΡΓΑΣΤΗΡΙΟ ΠΕΙΡΑΜΑΤΙΚΗΣ ΦΥΣΙΚΗΣ ΥΨΗΛΩΝ ΕΝΕΡΓΕΙΩΝ &
ΣΥΝΑΦΟΥΣ ΟΡΓΑΝΟΛΟΓΙΑΣ

Μελέτη της Εγκάρσιας Εκπεμψιμότητας και της Λαμπρότητας του **CERN PS Booster**

Διπλωματική Εργασία του:
Tirsi Prebibaj

Ακαδημαϊκός Επιβλέπων:	*Ερευνητική Επιβλέπουσα:*
Θεόδωρος Αλεξόπουλος	Δρ. Φανουρία Αντωνίου
Καθηγητής Ε.Μ.Π	Ερευνήτρια CERN

Αθήνα, 19 Σεπτεμβρίου 2019

Εθνικο Μετσοβιο Πολυτεχνειο
Σχολη Εφαρμοσμενων Μαθηματικων και Φυσικων Επιστημων
Τομεας Φυσικης
Εργαστηριο Πειραματικης Φυσικης Υψηλων Ενεργειων & Συναφους Οργανολογιας

Μελέτη της Εγκάρσιας Εκπεμψιμότητας και της Λαμπρότητας του **CERN PS Booster**

Διπλωματική Εργασία του:
Tirsi Prebibaj

Ακαδημαϊκός Επιβλέπων:	*Ερευνητική Επιβλέπουσα:*
Θεόδωρος Αλεξόπουλος	Δρ. Φανουρία Αντωνίου
Καθηγητής Ε.Μ.Π	Ερευνήτρια CERN

Εγκρίθηκε από την τριμελή εξεταστική επιτροπή στις 19 Σεπτεμβρίου 2019.

....	....	....
Θ. Αλεξόπουλος	Θ. Γέραλης	Φ. Αντωνίου
Καθηγητής Ε.Μ.Π.	Διευθυντής Ερευνών,	Ερευνήτρια CERN
	ΕΚΕΦΕ Δημόκριτος	

Αθήνα, 19 Σεπτεμβρίου 2019

....
Tirsi Prebibaj
Φυσικός Εφαρμογών Ε.Μ.Π.

Περίληψη

Έχει παρατηρηθεί πως υπάρχει μια αξιοσημείωτη ασυμφωνία στην εγκάρσια εκπεμψιμότητα μεταξύ των δεσμών που εξάγονται από τον PS Booster και εγχέονται στον PS σε συνθήκες λειτουγίας για τις δέσμες του LHC στο CERN. Ο PS Booster θα υποβληθεί σε μια σειρά από αναβαθμίσεις στα πλαίσια του LHC Injectors Upgrade (LIU) project με σκοπό την αύξηση της έντασης και της φωτεινότητας των παραδιδόμενων δεσμών. Οι απαιτήσεις του LIU όσων αφορά τις παραμέτρους των δεσμών θέτουν αυστηρά κριτήρια για τον υποβιβασμό τους κατά την διέλευσή από τους προεπιταχυντές και επιτρέπουν μια αύξηση στην εγκάρσια εκπεμψιμότητα μεταξύ του PSB και του PS μικρότερη του 5 %. Για αυτόν τον λόγο αυτή η ασυμφωνία πρέπει να γίνει κατανοητή. Συστηματικές μετρήσεις έχουν πραγματοποιηθεί ταυτόχρονα στους δύο επιταχυντές για αρκετά χαρακτηριστικά δεσμών (ένταση, εκγάρσια και διαμήκη εκπεμψιμότητα) χρησιμοποιώντας διάφορα ανεξάρτητα μετρητικά όργανα. Η μελέτη αυτή επικεντρώνεται στις επιπτώσεις που έχουν τα συστηματικά σφάλματα που προέρχονται από τις οπτικές παραμέτρους και το σχήμα της κατανομής της δέσμης στην λαμπρότητα στην έξοδο του PS Booster. Επιπλέον γίνεται μια αξιολογηση των μέθοδων που χρησιμοποιούνται για τον υπολογισμό της εκπεμψιμότητας με σκοπό την βελτιστοποίησή τους. Εξετάζονται επίσης τα αποτελέσματα και οι επιπτώσεις αυτών στο LIU project.

Abstract

A significant transverse emittance discrepancy is observed between the extraction of the PS Booster and the injection of the PS in operational conditions of the LHC beams at CERN. PS Booster will undergo a series of upgrades as part of the LHC Injectors Upgrade (LIU) project in order to increase the intensity and the brightness of the delivered beams. The LIU beam parameters require a tight budget for beam degradation along the injector chain and allow a PSB to PS transverse emittance growth of less than 5 %. For this reason this inconsistency needs to be understood. Systematic measurements were performed simultaneously in both machines with various beam characteristics (beam intensity, transverse and longitudinal emittance) and using various independent instruments. This study focuses on the impact of systematic errors that are induced by the optical parameters and the shape of the bunch distribution on the brightness at the extraction of the PS Booster. Furthermore, an evaluation and optimization of the methods that are used to calculate the emittance is made. The results and their impact on the LIU project are discussed.

Acknowledgements

I would like to express my gratitude to all the people who supported and helped me during this last year.

This thesis wouldn't be possible without the contribution of my supervisor Dr. Fanouria Antoniou. I am deeply thankful to her for giving me the opportunity to join CERN, for her willingness to guide and motivate me in my first steps of my scientific career and for carefully reading and correcting this thesis. She is a great scientist, an exceptional mentor and most of all a kind person.

I would like to thank my university advisor Prof. Theodoros Alexopoulos for his continuous help and support whenever needed.

I want to show my appreciation to all my colleagues of the BE-ABP-HSI section. Being part of this great team was a remarkable and very beneficial experience for me. Special gratitude to Hannes Bartosik for sharing his immense knowledge and to Gian Piero Di Giovanni whose positiveness and comments on my early work motivated me further.

On a personal level I thank my friends Michalis, Natalia and Sofia for all the discussions and the enjoyable coffee brakes in building 6 and also Angelos, Athina, Christos, Dimitris and Spyros for all the great time we had both in Athens and Geneva.

The time spend outside work wouldn't be that pleasant if there wasn't for Thenia. Always being there for me, with a cheerful mood, she was the best companion I could ask for in this unique experience.

Finally, there are no words express my gratitude to my parents and to my precious sister Tiona. So far yet so close to me, they always reminded me what is important in life through their endless love and support.

Contents

List of Figures

List of Tables

Chapter 1

Introduction

Particle accelerators are machines that accelerate charged particles using electromagnetic fields. The history of modern particle accelerators dates back to the first half of the 20th-century. Since then many accelerator types were designed and constructed from Cyclotrons to Linear accelerators (Linacs), Synchrocyclotrons, Synchrotrons and Particle Colliders. Today their size and performance varies enormously with numerous applications in research and industrial fields such as experimental particle and nuclear physics, condensed matter physics, biology, material processing, production of radioisotopes and radiotherapy, which makes them one of the most useful modern human inventions.

1.1 The CERN Accelerator Complex

Currently the world's largest and most powerful accelerator is the Large Hadron Collider (LHC) [1]. The LHC is a circular particle accelerator collider built at CERN [2] between the Franco-Swiss border. It has a circumference of 27 km and it is designed to accelerate proton and/or ion beams from 450 GeV to 7 TeV. The beams travel in opposite directions through separate beam pipes and collide at four interaction points (IPs). Around the IPs large particle detectors have been placed: ATLAS, CMS, ALICE and LHCb, which measure the outcome of these collisions in the form of new particles.

Before injection into the LHC, the beams are produced and gradually accelerated up to 450 GeV by a series of smaller accelerators, known as the LHC injector complex [3] (Fig. 1.1). Protons are produced by stripping the electrons of hydrogen atoms inside a bottle of hydrogen gas using an electric field. The first part of the accelerator chain is the Linac2 which accelerates the protons to a kinetic energy of 50 MeV. These particles are then injected into the Proton Synchrotron Booster (PSB) and their energy is increased up to 1.4 GeV. Afterwards, the beam travels through the Proton Synchrotron (PS), where it reaches an energy of 25 GeV, followed by the Super Proton Synchrotron (SPS) which accelerates them up to 450 GeV. Finally the protons are injected into the LHC. The lead-ion beams start from Linac3, which injects them into the Low Energy Ion Ring (LEIR) and later on they successively travel into the PS, the SPS and the LHC.

CERN operates also other accelerators, such as the Anti-proton Decelerator (AD)

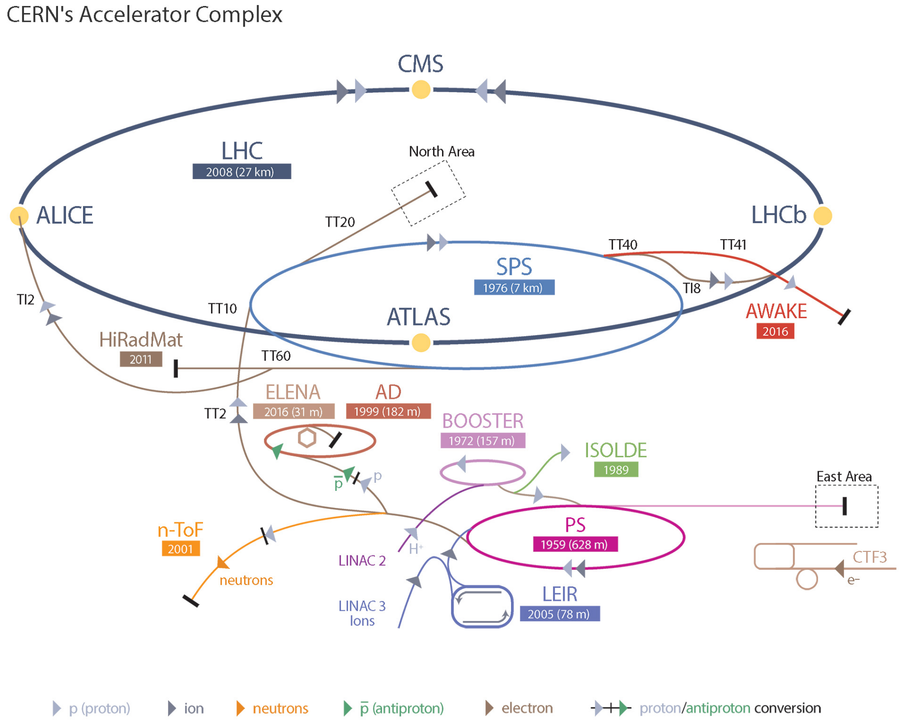

Figure 1.1: A schematic of the accelerator complex at CERN

that produces low-energy antiprotons for studies of antimatter, and many physics facilities that receive beams for fixed target experiments such as the on-line isotope mass separator (ISOLDE) facility, the neutron Time Of Flight facility (nTOF) and more. This study will focus on the Proton Synchrotron Booster.

1.2 The Proton Synchrotron Booster

The Proton Synchrotron Booster (PSB) [4] is a proton circular accelerator located at CERN. It was built between 1968-1972 with the center of the machine placed exactly on the Franco-Swiss border. Its construction posed many technological challenges at that time due to its unique 4-ring design. Today it is used as an injector to the Proton Synchrotron but also delivers high intensity beams to the ISOLDE facility. The PS Booster provides a wide range of intensity, energy and time structure beams making it an extremely flexible machine. It lays between the Linac2 and the PS in the CERN's accelerator complex (Figure 1.1).

PSB consists of four superposed rings, with a radius of 25 meters each, that have a common injection and extraction beam line. Particles are injected from Linac2 to each ring through a vertical distribution system consisting of a series of kicker [5] and septum magnets [6]. Each ring is divided into 16 periods of 9.8 m each, meaning that the same magnetic elements are repeated in every period (“super periodicity” of 16). Figure 1.2 shows the layout of the PSB.

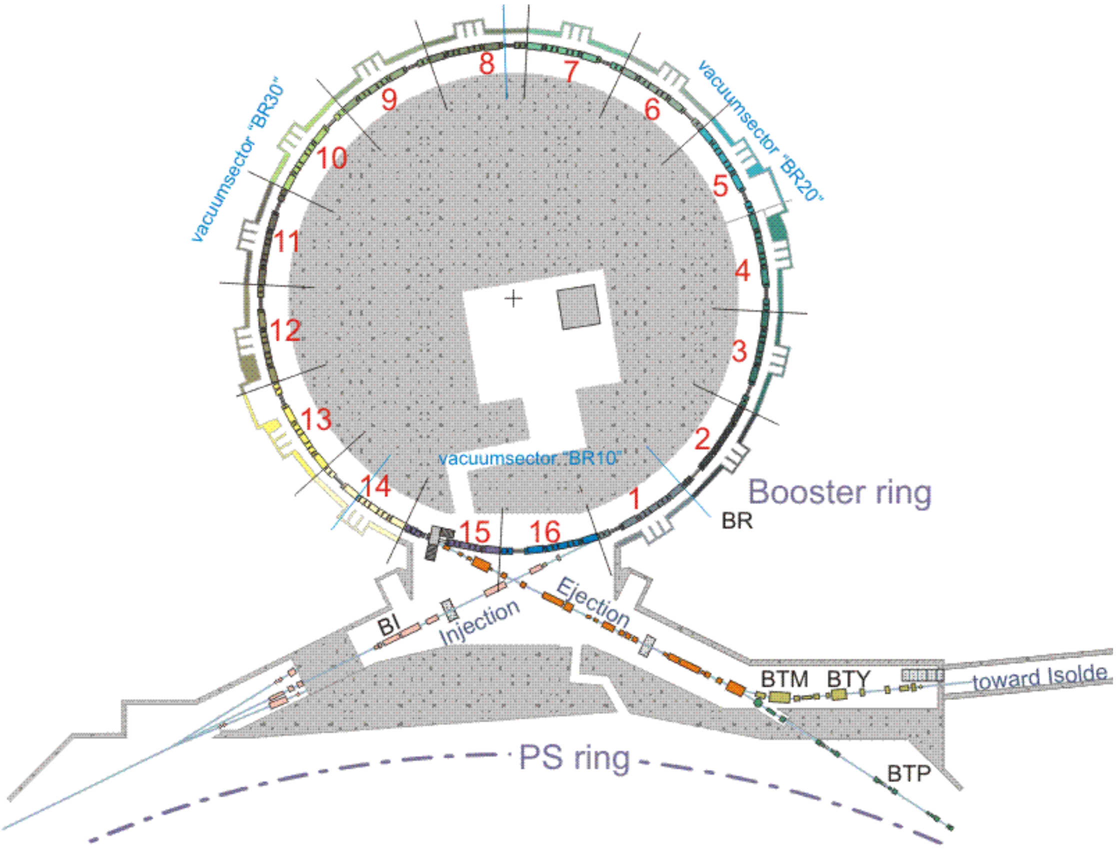

Figure 1.2: PSB Layout

Figure 1.3 shows a schematic layout of one PSB period (here period 2). Each period consists of two bending units, one focusing unit and a straight section that is used for other insertions like beam instrumentation and diagnostics. The straight section of this particular period contains a Wire Scanner [7] (FWS.2L2). A Wire Scanner (WS) is an instrument that measures the transverse beam profiles of a beam. This device is used extensively in this study for the emittance measurements.

The PSB is a fast-cycle accelerator with a basic period of 1.2 seconds. The injection starts at 275 ms and the extraction at 805 ms. The different cycles are completely independent from each other and follow a predefined super-cycle which is repeated many times (pulse-by-pulse modulation). Figure 1.4 [8] shows the relativistic factors along the PSB cycle. The two dashed lines represent the injection and the extraction time. The revolution frequency is 0.6 MHz at injection energy and 1.7 MHz at extraction energy.

Before extraction the bunches in the four rings are synchronized, recombined and then extracted, allowing the delivery to the PS of 4 times the intensity for each pulse of the Linac2. The bunches are extracted by a system of slow bumpers [9] and then

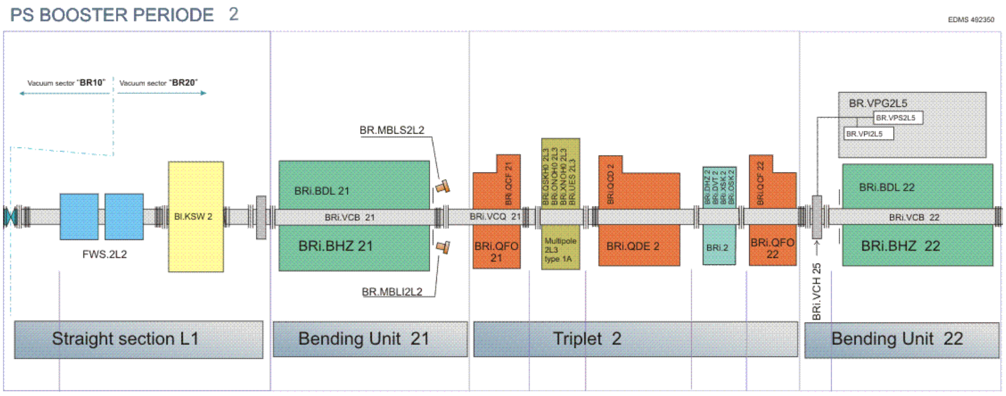

Figure 1.3: PSB Period 2

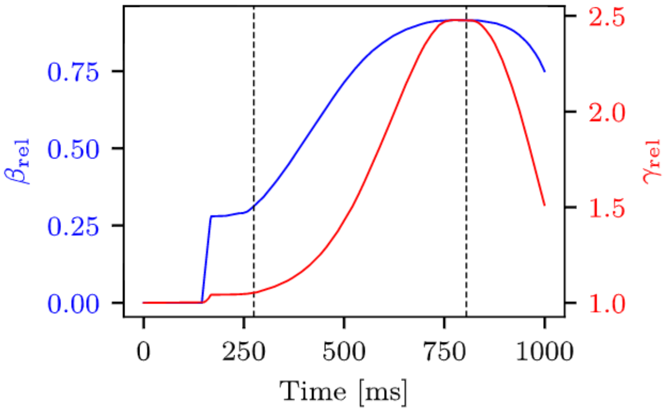

Figure 1.4: PSB cycle relativistic factors

are recombined by a system of vertical kickers and septa (BT transfer line). After the recombination the bunches can go either towards the PS through the Booster-to-PS (BTP) transfer line or towards the measurement line (BTM). In the BTM line the bunches can either follow the Booster-to-Isolde (BTY) transfer line or they can end up to a beam dump after passing through a series of beam instrumentation devices. Figure 1.5 shows a schematic layout of the BTM transfer line. The three horizontal and vertical Secondary Emission Monitors (BTM.SGHi and BTM.SGVi) [10] are located before the beam dump and are used to measure beam density profiles from which the beam size and eventually the emittance can be derived. The Secondary Emission Monitors (SEM Grids) are also used extensively in this study.

All rings of the PSB are equipped with three RF cavities. The first two (C02 and C04) are used for acceleration on harmonic numbers $h = 1$ and $h = 2$ respectively, while the third one (C16), which has a higher frequency than the other two, is used for controlling the longitudinal emittance blow-up [9]. Applying both $h = 1$ and $h = 2$ systems the spacing and the flattening of the bunches can be adjusted [9]. This way the bunching factor [11] can be maximized and the peak line density minimized.

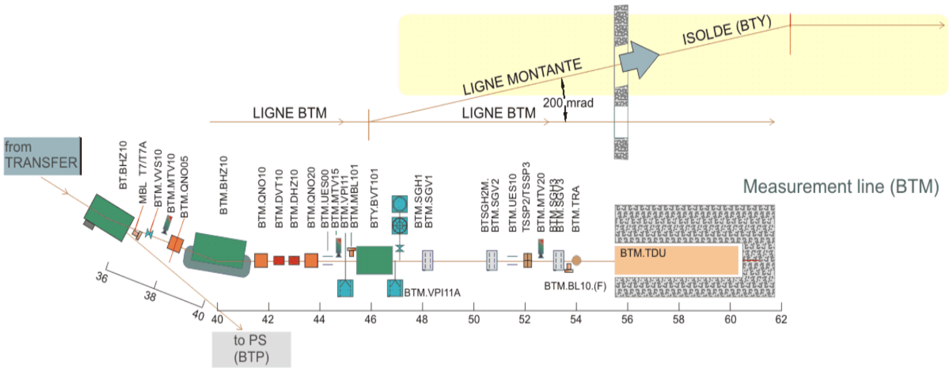

Figure 1.5: BTM transfer line

Throughout the years of operation PSB went through a series of upgrades in order to increase the intensity, the brightness and the energy of the machine. Although its design top energy was 800 MeV two upgrades increased it to 1.0 GeV and after to 1.4 GeV (today's operation). In terms of intensities the PSB can operate in a wide spectrum, from $5 \cdot 10^9$ to $4 \cdot 10^{13}$ particles per bunch (ppb), to produce high and intermediate intensity beams to the PS and the SPS for the fixed-target physics, high intensity beam to the ISOLDE facility or high-brightness beams for the LHC.

1.3 The LHC Injectors Upgrade Project

The requirements of the High Luminosity LHC (HL-LHC) Project [12] exceed the so-far performances of the accelerator's complex. The current injected beam intensity of the LHC needs to be doubled while the brightness to be multiplied by a factor of 2.5. The LHC Injectors Upgrade (LIU) Project [13] aims to upgrade all the LHC injectors in order to fulfill the HL-LHC requests. The LIU started at the beginning of 2019 and it will continue during the two-year Long Shutdown 2 (LS2) phase of the accelerator complex. During this period the PSB will undergo a series of substantial upgrades in the framework of LIU which can be classified mainly in two parts:

- Upgrade of the injection line to accommodate the new 160 MeV H^- injection scheme [14] from Linac4 [15]

- Upgrade of the ring and the extraction line to permit the increased extraction energy from 1.4 GeV to 2.0 GeV.

Linac2 was the injector of the PS Booster since 1978 but in 2020 will be replaced by the Linac4. The Linac4 will inject H^- beams at the energy of 160 MeV (instead of the previous 50 MeV) allowing the increase of the beam brightness of the PSB. In the rings and in the extraction line many hardware upgrades are currently in progress. Most of the magnets will be modified or replaced in order for the 2 GeV beams to be accommodated.

New instrumentation for the high brightness beams will be installed (for example a new generation of Wire Scanners). Electrical and vacuum systems and power converters will also be modified.

1.4 Aim and Outline of the Thesis

Accelerators pose a set of challenges that require a considerable amount of effort, time and careful attention of the people that design, construct and operate them. For example manufacturing errors of the magnets or the non-perfect vacuum inside the beam pipes can lead to undesired effects on the beam or to reduction of the beam quality and lifetime. But not only mechanical imperfections can complicate the operation of the machine. Particles inside beams create electromagnetic fields that act upon themselves or interact with the surrounding environment (beam pipe walls). These can cause many beam instabilities and limit the performance of the machine. Many studies are dedicated in dealing with these matters in order to expand the capabilities of the machines and also to reveal new aspects of the physics behind accelerators.

This thesis is the subject of a similar study that took place at the PS Booster. A significant emittance discrepancy is observed between the PSB extraction and the PS injection in operational conditions. The LIU requires an emittance growth of less than 5 % between the two machines [16] and therefore this inconsistency needs to be understood. Through this study the emittance at the extraction of the PSB and its behaviour under different beam conditions is inspected. Systematic emittance measurements have been performed in the PSB rings and the BTM transfer line by using different instruments, beam intensities and computation algorithms. The measurements are presented and then the impact of possible sources of systematic errors is investigated.

The thesis can be divided in two parts: the first part consists of Chapters 2 and 3. Chapter 2 aims to introduce the necessary theoretical concepts that this study relies on. A brief introduction to the linear beam dynamics is made through which the emittance is defined. Chapter 3 describes the techniques that were used to measure the emittance. Particular attention has been given in explaining step-by-step the whole calculation process, starting from the measured data to the final emittance values.

The second part consists of Chapters 4 to 6. Chapter 4 reports the observations from previous years about the PSB-PS emittance discrepancy and constitutes the initial motivation of carrying out this study. Then it continues on presenting the measurement of the optical parameters: the dispersion and the beta function. These measurements reveal the impact of the systematic errors on the emittance at extraction of the PSB. In Chapter 5 the systematic errors that the emittance computation algorithms induce are developed by modeling the relation between the bunch distributions. Afterwards the measurements are benchmarked with this model and the importance of the deconvolution algorithms in the view of the LIU project is discussed. Finally Chapter 6 summarizes and reviews all the measurements and the results of this study.

Chapter 2

Concepts of Beam Dynamics

The area of physics that studies the accelerators is called Accelerator Physics. Accelerator physics is a developing field which involves many other topics such as electromagnetism, quantum mechanics, nonlinear dynamics and condensed matter physics. In this chapter will be given an overview of some basic concepts of beam dynamics in synchrotrons. The physical principles behind the transverse and longitudinal motion are introduced together with the definitions of the Twiss parameters, the emittance, the dispersion, the brightness and their properties. These definitions will be accompanied by examples from the PS Booster.

2.1 Synchrotrons

Synchrotrons have a circular shape and the accelerated particles follow a closed-loop path, allowing the use of the same accelerating structures many times and therefore reaching to very high energies. The interaction between the charged particles and the electromagnetic fields is governed by the Lorentz force:

$$\vec{F}_L = q(\vec{E} + \vec{v} \times \vec{B}), \tag{2.1}$$

where q is the charge of the particle, $\vec{v}$ is the velocity vector of the particle and $\vec{E}$, $\vec{B}$ are the electric and magnetic field vectors respectively. The electric fields are used to increase the energy of the particles (accelerate) while the magnetic fields, since they act orthogonal to the direction of motion, to manipulate their trajectories.

The equations of motion inside any general electromagnetic field can be found by substituting the Lorentz force into the relativistic third law of Newton. For example, a particle inside a uniform magnetic field perpendicular to its velocity will move on a circular arc, with a bending radius ρ equal to [17]:

$$\rho = \frac{p}{qB}, \tag{2.2}$$

where p is the momentum, q is the charge and B is the strength of the magnetic field. Since the radius of a Synchrotron is constant, in order to keep the particles in the desired trajectory, the ratio p/B must also remain constant. In other words the magnetic field B must increase synchronously with the momentum p of the accelerated particle (hence the name “synchrotron”).The quantity $(B\rho)$ is very often used and it is known as the “beam magnetic rigidity”. In practical units it is expressed as:

$$(B\rho)[T\cdot m] \approx \frac{p[GeV/c]}{0.2998\cdot q[e]}. \tag{2.3}$$

The particle trajectory that closes to itself after a complete revolution is known as the “closed orbit”.

Synchrotrons are composed of elements such as RF-cavities which provide the necessary energy to the particles, dipole magnets that produce the uniform magnetic fields, quadrupole magnets in order to keep the particles tightly confined within a finite space (focused), sextupole, octupole (or higher order) magnets to correct undesired effects, beam diagnostics and many more. The beam pipe that surrounds the particles is usually in high vacuum conditions.

2.2 Frenet-Serret Reference System

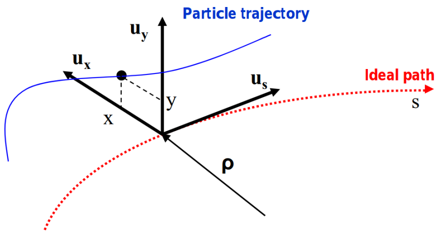

Figure 2.1: Frenet-Serret Reference Frame

Since the particle trajectory inside a synchrotron is curved one must use an appropriate coordinate system than will simplify the equations of motion. Instead of the Cartesian coordinates, a more convenient system to use is the Frenet-Serret reference frame [18]. The origin of the frame moves along the ideal path (orbit) of the reference particle (Figure 2.1). This path is fixed by the construction of the synchrotron.

For any time t the particle has a unique position along the longitudinal spatial coordinate s. In accelerators all derivatives are expressed with respect to s instead of t. At each s-position the state of any particle is represented by a 6-dimensional vector:

$$(x, x', y, y', s, \delta). \tag{2.4}$$

The (x, y, s) are the three spatial coordinates of the particle and the (x', y') the derivatives of these coordinates with respect to s. The variable δ is the relative momentum offset from the momentum of the reference particle:

$$\begin{aligned} x' &:= \frac{dx}{ds} = \frac{dx}{dt}\frac{dt}{ds} = \frac{v_x}{v_s} = \frac{p_x}{p_s} \approx \frac{p_x}{p_0}, \\ y' &:= \frac{dy}{ds} = \frac{dy}{dt}\frac{dt}{ds} = \frac{v_y}{v_s} = \frac{p_y}{p_s} \approx \frac{p_y}{p_0}, \\ \delta &:= \frac{\Delta p}{p_0} = \frac{p-p_0}{p_0}, \end{aligned} \tag{2.5}$$

where p_0 is the reference (design) momentum of the reference particle. The approximation that the transverse momentum is very small in comparison to the longitudinal momentum is made (paraxial approximation $p_s \approx p_0 >> p_x, p_y$). This assumption is valid for the majority of cases in synchrotrons since the particles are travelling with ultra relativistic speeds around the machine. When discussing the dynamics of the transverse plane, if not otherwise stated, the two transverse planes (the x-x' and y-y' variables) will be both represented using the characters u-u'.

2.3 Magnetic Elements

In order to control the trajectory of the particles inside a synchrotron several magnetic components are used. Dipole (or bending) magnets are installed in order to keep the particles in a circular motion. A dipole magnet creates a uniform magnetic field in the vertical plane (B_y) perpendicular to the particle's velocity (v_s). The resulting force will be perpendicular to both the velocity and the magnetic field (cross product in eq. 2.1), thus pointing towards the center of the machine and forcing the particle to perform a stable circular motion:

$$\vec{F}_L = (v_s \hat{s}) \times (B_y \hat{y}) = -v_s B_y \hat{x} \equiv -F_x \hat{x}. \tag{2.6}$$

The ideal orbit of the reference particle is defined by the arrange of the dipoles in the machine. For a ring with N identical dipoles the bending angle of each magnet can be found using the relation:

$$\theta = \frac{2\pi}{N}, \tag{2.7}$$

since the total bending angle must be 2π rad. The bending radius of each dipole therefore is:

$$\rho = \int \frac{ds}{\theta} \approx \frac{l_d}{\theta}, \tag{2.8}$$

where the integration is made along the particle path and l_d is the physical length of the dipole. Consequently, from equations (2.7), (2.8) and (2.3), the higher the strength of the magnetic field of the dipoles the smaller the ring circumference is (or smaller is the number of dipoles that have to be used), for a constant energy (momentum) of the particles. Figure 2.2 (left) shows the top-view of the curved path that a particle follows inside a dipole.

In reality, particles always have a small angular divergence from the ideal orbit which can result, after some turns, in hitting the walls of the beam pipe and eventually being lost. For this reason quadrupole magnets are also installed in order to repeatedly steer (focuse) the particles back to the reference orbit. A quadrupole magnet produces a magnetic field that is growing with the distance from the longitudinal axis, which is set to be the reference orbit. Figure 2.2 (right) shows the magnetic field inside a quadrupole magnet. Solving the Maxwell's equations inside the magnet results to a magnetic potential of the form:

$$\psi = gxy, \tag{2.9}$$

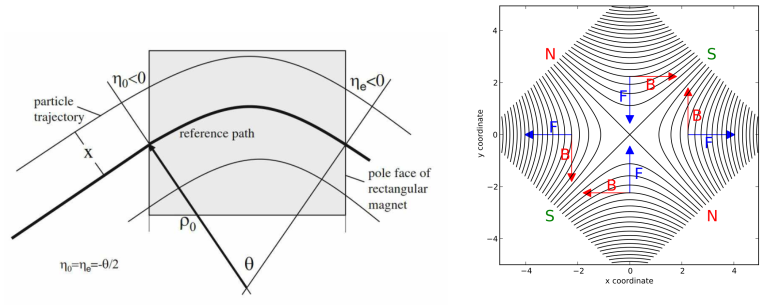

Figure 2.2: Dipole (left) and Quadrupole (right) magnets

where g the gradient of the quadrupole magnet [17] with units of T/m. By the definition of the potential, the magnetic field vector will be:

$$\vec{B} = (B_x, B_y) = \nabla\psi = g(y, x) \tag{2.10}$$

and therefore the Lorentz force for a particle moving along the longitudinal axis with a velocity v (eq. 2.1):

$$\vec{F}_L = q \cdot v \cdot g(x, -y), \tag{2.11}$$

will linearly increase with the distance from this axis. The particles that are further away from the reference orbit feel stronger forces than those that are closer. The direction of the force will face towards the center of the magnet (focusing) in the vertical plane, while in the horizontal plane will face towards the poles of the magnet (defocusing).

For a quadrupole that is rotated 90 degrees with respect to its longitudinal axis, the focusing and defocusing planes are inverted. In order to achieve a total focusing in the two transverse planes, both quadrupole types are placed with carefully chosen distances in-between them (alternating gradient focusing). The gradient g over the magnetic rigidity is defined as the normalized focusing strength:

$$k = \frac{g}{B\rho} \tag{2.12}$$

with units of m^{-2}.

The resulting forces of the dipoles and the quadrupoles are either constant or depend linearly with the transverse displacement from the ideal trajectory. In this study only the dynamics behind the beam steering and focusing due to these elements will be considered (linear transverse beam dynamics). The fields of these elements are assumed to end abruptly at the edges of the magnets (hard-edge model [17]). In general other non-linear magnetic components are also used (sextupoles, octupoles etc.), usually for field corrections, but they will not be considered here. In the case of the PSB, each ring consists of a total of 32 dipole and 48 quadrupole magnets.

2.4 Transverse Beam Dynamics

2.4.1 Hill's Equations

Having established a convenient reference frame one has to express the Newton's third law with the Lorentz force using the coordinates of this frame. It is assumed that the velocity of the particles changes slowly while they pass through the magnetic elements and the momentum deviation of the particles is relatively small (less than 1 %) [17]. This allows a linear Taylor approximation of the particle momentum in terms of the momentum offset. Using the properties of the rotated coordinate system one can obtain the equations of motion for any particle travelling through an arbitrary periodic magnetic structure of dipoles and quadrupoles. These equations are second order linear differential equations and are known as the Hill's Equations [17, 19, 20]:

$$\frac{d^2u}{ds^2} + K_u(s)u(s) = \delta_D(u-x)\frac{1}{\rho(s)}\frac{\delta p}{p}, \quad u = x \; or \; y, \tag{2.13}$$

where:

$$K_u(s) = \begin{cases} \frac{1}{\rho(s)} + k(s), & \text{if } u = x \\ -k(s), & \text{if } u = y \end{cases} \tag{2.14}$$

is the periodic non-constant restoring force due to the magnetic elements (dipoles and quadrupoles) of the accelerator, $\rho(s)$ is the local bending radius of the reference orbit, $\delta p/p$ is the momentum offset of the particle with respect to the nominal momentum of the reference particle and $\delta_D(u-x)$ the Dirac delta function. The longitudinal position s of the particle is used as the independent variable instead of the time t. Initially only the on-momentum particles will be considered, thus particles with $\frac{\delta p}{p} = 0$. The effects of a non-zero momentum offset will be discussed in Chapter 2.4.4.

The term $k(s)$ in eq. (2.14) is due to the focusing of the quadrupoles and has a different sign in the two planes since a focusing quadrupole in one plane is a defocusing in the other. The other term ($\rho(s)^{-1}$) comes from the dipoles. Despite the fact the dipoles have no focusing field gradient the particles are actually focused due to the circular movement inside the uniform magnetic field. Particles that enter the dipole with small horizontal offsets with respect to each other will follow circular orbits that will approach or even cross each other (Fig. 2.3). In large machines this effect is very weak and it is known as the "weak focusing" while the focusing of the quadrupoles is called the "strong focusing".

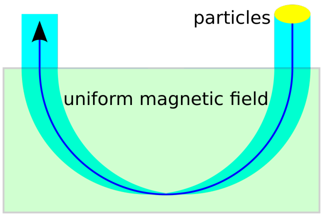

Figure 2.3: Weak focusing

Using Floquet's theorem [20] the analytical solution of the (homogeneous) equation of motion can be expressed using the Courant-Snyder parametrization [20]:

$$u(s) = \sqrt{2J_u\beta_u(s)}\cos\left(\int_0^s \frac{1}{\beta_u(s)}ds + \phi_{u,0}\right) \equiv w_u(s)cos(\phi_u(s) + \phi_{u,0}), \tag{2.15}$$

where:

- J_u, $\phi_{u,0}$ are fixed integration constants which depend on the initial conditions of the particle. The initial amplitude J_u has units of length and it is known as the "action". In some textbooks the term "single particle emittance" $\epsilon_u \equiv 2J_u$ is also used.
- $\beta_u(s)$ has units of length and it is called the amplitude or beta function. The beta function is a periodic function in the synchrotron's perimeter and it depends only on the magnetic structure ("lattice") of the accelerator.
- $\phi_u(s) := \int_0^s \frac{1}{\beta_u(s)} ds$ is called betatron phase advance between points 0 and s.
- $w_u(s) \equiv \sqrt{2J_u\beta_u(s)}$ is known as the envelope of the beam.

This solution describes a transverse oscillation, known as the "betatron oscillation", around the closed orbit, whose amplitude $w_u(s)$ and phase $\phi_u(s)$ depend on the s-position. These quantities are also defined:

- $\alpha_u(s) := -\frac{1}{2}\frac{d\beta_u}{ds}$ known as the alpha Twiss function and has no physical units.
- $\gamma_u := \frac{1+\alpha_u^2}{\beta_u}$ known as the gamma Twiss function with units of inverse length.
- $Q_u := \frac{1}{2\pi}\oint \frac{ds}{\beta_u(s)} \equiv \frac{\mu_{u,turn}}{2\pi}$ called the betatron tune. It describes the number of betatron oscillations that a particle performs during one complete revolution around the machine. The horizontal and vertical tune in the tune-space is known as the working point. In the PSB the current working point at injection is $(Q_H, Q_V) = (4.28, 4.47)$ and at extraction $(Q_H, Q_V) = (4.17, 4.23)$ (Q4Q4 optics).

The three functions $\beta_u(s)$, $\alpha_u(s)$ and $\gamma_u(s)$ are called Twiss parameters (functions). Figure 2.4 shows horizontal and vertical alpha and beta Twiss functions of the Booster as a function of the s-position. A more detailed derivation of the Twiss functions can be found in [21]. Later, this solution is used to represent not only the dynamics of a single particle but also the whole beam.

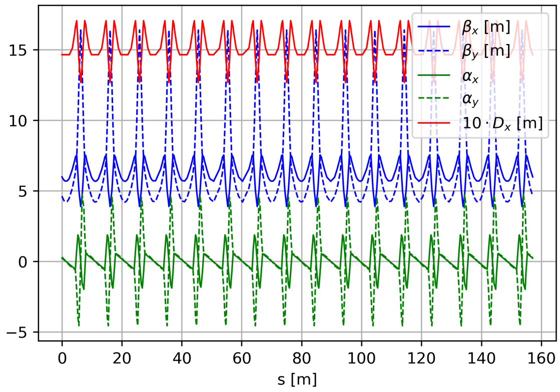

Figure 2.4: PSB model optics functions

The dynamics of the particles inside an accelerator can be studied through their phase space plot. The derivative of the solution $u(s)$ with respect to s is:

$$u'(s) = -\frac{\sqrt{2J_u}}{\sqrt{\beta_u(s)}}[\alpha_u(s)\cos(\phi_u(s) + \phi_{u,0}) + \sin(\phi_u(s) + \phi_{u,0})], \tag{2.16}$$

Eliminating the $\phi_u(s)$ from the $u(s)$ and $u'(s)$ functions one obtains the $u(s) - u'(s)$ relation:

$$\gamma_u(s)u(s)^2 + 2\alpha_u(s)u(s)u'(s) + \beta_u(s)u'(s)^2 = 2J_u. \tag{2.17}$$

This is a parametric representation of a family of ellipses with a parameter s. Therefore the phase space of a single particle inside an accelerator in any s-position is represented by an ellipse. This relation reveals that the "action" is more than an initial condition: it is related to the (constant) area of this phase space ellipse with a factor of π:

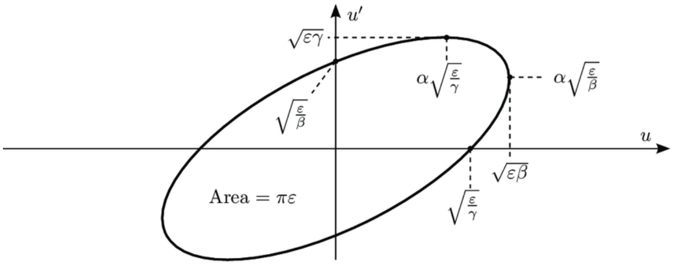

Figure 2.5: Phase space of a single particle

$$(Area) = 2J_u \cdot \pi \tag{2.18}$$

The "action" is an invariant of the motion and it is also known as the Courant-Snyder invariant. The importance of the Twiss parameters is also clear: they represent the geometric parameters that define the shape and the orientation of the ellipse. Figure 2.5 shows the phase space ellipse of a single particle. The symbol ϵ refers to the single particle emittance (action). The values that are noted in this figure can be found with simple algebraic calculations. Equation (2.17) can be re-written using matrix formalism as follows:

$$\begin{bmatrix} u & u' \end{bmatrix} \begin{bmatrix} \beta_u & -\alpha_u \\ -\alpha_u & \gamma_u \end{bmatrix} \begin{bmatrix} u \\ u' \end{bmatrix} \equiv UB_u(s)U^T = J_u. \tag{2.19}$$

The matrix $B_u(s)$ is called Beta or Twiss matrix.

Summarizing, the transverse dynamics of a particle inside a set of quadrupoles and dipoles are described by the Hill's equation. The solution of this equation is an s-dependent oscillation around the reference orbit which can be parameterized using the Twiss parameters. The phase space of the particle is an ellipse whose shape is determined by the Twiss parameters. Also each particle is associated with an invariant of the motion, the action, which corresponds to the area of this phase space ellipse.

2.4.2 Matrix Notation

The formalism that has been developed so far is expressed in terms of the Twiss parameters. For a particle that travels from $s_1 = 0$ to s_2 with known initial conditions at $s = s_1 : u = u_1, u' = u'_1$ and $\phi_u(s = s_1) = 0$, using equations (2.15) and (2.16), one finds:

$$\begin{aligned} \cos\phi_{u,0} &= \frac{u_1}{\sqrt{J_u\beta_1}}, \\ \sin\phi_{u,0} &= -\frac{1}{\sqrt{J_u}}(u'_1\sqrt{\beta_1} + \frac{\alpha_1 u_1}{\sqrt{\beta_1}}). \end{aligned} \tag{2.20}$$

Substituting these expressions again to equations (2.15) and (2.16) and using a few trigonometric identities, the u and u' at the position $s = s_2$ can be written in the form of:

$$\begin{bmatrix} u_2 \\ u_2' \end{bmatrix} = \begin{bmatrix} \sqrt{\frac{\beta_2}{\beta_1}}(\cos\Delta\mu + \alpha_1 \sin\Delta\mu) & \sqrt{\beta_2\beta_1}\sin\Delta\mu \\ -\sqrt{\beta_2\beta_1}[(1+\alpha_1\alpha_2)\sin\Delta\mu + (\alpha_2 - \alpha_1)\cos\Delta\mu] & \sqrt{\frac{\beta_1}{\beta_2}}(\cos\Delta\mu - \alpha_2\sin\Delta\mu) \end{bmatrix} \begin{bmatrix} u_1 \\ u_1' \end{bmatrix}. \tag{2.21}$$

where $\Delta\mu \equiv \phi_u(s_2)$. This matrix is called the Twiss Transfer Matrix. The Twiss functions depend on the configuration of the magnets throughout the accelerator. In this chapter the connection between the lattice of the accelerator and the Twiss functions will be demonstrated using matrix formalism.

Assuming an accelerator that consists of only a single focusing quadrupole of a constant strength $k > 0$ and considering only the horizontal plane (weak focusing effects are neglected) the Hill's equation is simplified to the one of a simple harmonic oscillation:

$$\frac{d^2x(s)}{ds^2} + kx(s) = 0, \tag{2.22}$$

with a solution:

$$\begin{aligned} x(s) &= A\cos\sqrt{k}s + B\sin\sqrt{k}s, \\ x'(s) &= -A\sqrt{k}\cos\sqrt{k}s + B\sqrt{k}\sin\sqrt{k}s. \end{aligned} \tag{2.23}$$

If the initial conditions of the particle where $x(0) = x_0$ and $x'(0) = x_0'$ the solutions can also be written in matrix notation:

$$\begin{bmatrix} x(s) \\ x'(s) \end{bmatrix} = \begin{bmatrix} \cos\sqrt{k}s & \frac{1}{\sqrt{k}}\sin\sqrt{k}s \\ -\sqrt{k}\sin\sqrt{k}s & \cos\sqrt{k}s \end{bmatrix} \begin{bmatrix} x_0 \\ x_0' \end{bmatrix} \equiv M_{QF} \begin{bmatrix} x_0 \\ x_0' \end{bmatrix}. \tag{2.24}$$

The matrix M_{QF} is defined as the matrix of a quadrupole of strength k. If the particle was initially (before the quadrupole) at x_0 with a momentum of x_0', after the quadrupole the particle is at $x(s)$ with a momentum of $x'(s)$. Similar analysis can be applied in the vertical plane but this time the sing of the quadrupole strength is negative. This leads to a defocusing beam and so the cosine and sine functions are replaced with the hyperbolic cosine and sine functions (*cos* ↔ *cosh* and *sin* ↔ *sinh*).

Using an analogous procedure one can obtain the matrix for a single dipole of length l_d and a bending angle of θ:

$$M_{dipole} = \begin{bmatrix} \cos\theta & \rho\sin\theta \\ -\frac{1}{\rho}\sin\theta & \cos\theta \end{bmatrix}, \tag{2.25}$$

where $l_d = \rho\theta$ (eq. 2.8), and also the matrix of a single drift space of length d:

$$M_{drift} = \begin{bmatrix} 1 & d \\ 0 & 1 \end{bmatrix}. \tag{2.26}$$

The transfer matrix of any interval throughout the accelerator is simply the product of the transfer matrices of all the elements that this interval contains (a drift space is considered also as an element). If for example between the positions $s = s_1$ and $s = s_2$ there are N elements then:

$$\begin{bmatrix} u_2 \\ u_2' \end{bmatrix} = M_N \cdot M_{N-1} \cdot ... \cdot M_1 \begin{bmatrix} u_1 \\ u_1' \end{bmatrix} \equiv \begin{bmatrix} m_{11} & m_{12} \\ m_{21} & m_{22} \end{bmatrix} \begin{bmatrix} u_1 \\ u_1' \end{bmatrix} \equiv M_{s_1 \to s_2} \begin{bmatrix} u_1 \\ u_1' \end{bmatrix}. \tag{2.27}$$

Comparing the elements of this transfer matrix with the Twiss transfer matrix of eq. (2.21) one can numerically find the Twiss parameters at the positions s_1 and s_2 and in general at any position of the accelerator. By changing the magnets strength and their relative distances the optical parameters can be optimized in order to control the transverse motion of the particles. The elements of the second row of the transfer matrix are the derivatives of the first row with respect to the parameter s [22]. So usually the notation $m_{11} \leftrightarrow C$, $m_{12} \leftrightarrow S$, $m_{21} \leftrightarrow C'$, $m_{22} \leftrightarrow S'$ is used.

2.4.3 Emittance

A beam from a synchrotron consists of many particles. In the PSB for example an LHC beam typically consists of 10^{10} particles. As a first approximation only particles that are independent of each other will be considered, meaning that they do not interact. In reality the particles, being charged, they interact with each other in many ways with the Coulomb forces. These interactions go beyond the scope of this study so they will be neglected. The distribution of the particles is assumed to be Gaussian in order to simplify the analytical calculations.

The methodology that was presented in the previous chapters for a single particle applies for any particle of a bunch. Each one of them makes a betatron oscillation around the reference orbit and has its own ellipse with a constant invariant. These ellipses have different areas due to different actions, which depend on the initial conditions of each particle. But the orientation of these ellipses are all the same at a specific position of the accelerator, because they depend only on the Twiss parameters. The phase space of a Gaussian bunch looks similar to Figure 2.6.

For the distribution of particles the Sigma matrix is defined as:

$$\Sigma_{u,RMS} = \begin{bmatrix} < u^2 > & < uu' > \\ < uu' > & < u'^2 > \end{bmatrix} \equiv \begin{bmatrix} \sigma_u & \sigma_{uu'} \\ \sigma_{uu'} & \sigma_{u'} \end{bmatrix}, \tag{2.28}$$

where its elements are the second order moments of the u and u' distributions:

$$< uu' > = \frac{1}{N_p} \sum_{i=1}^{N_p} (u_i - \overline{u})(u_i' - \overline{u}'). \tag{2.29}$$

N_p is the number of particles inside the bunch called intensity or beam population. The top left element of the Sigma matrix, σ_u, is defined as the Root Mean Square (RMS) bunch (beam) size. Figure 2.6 shows the RMS beam size in the horizontal histogram

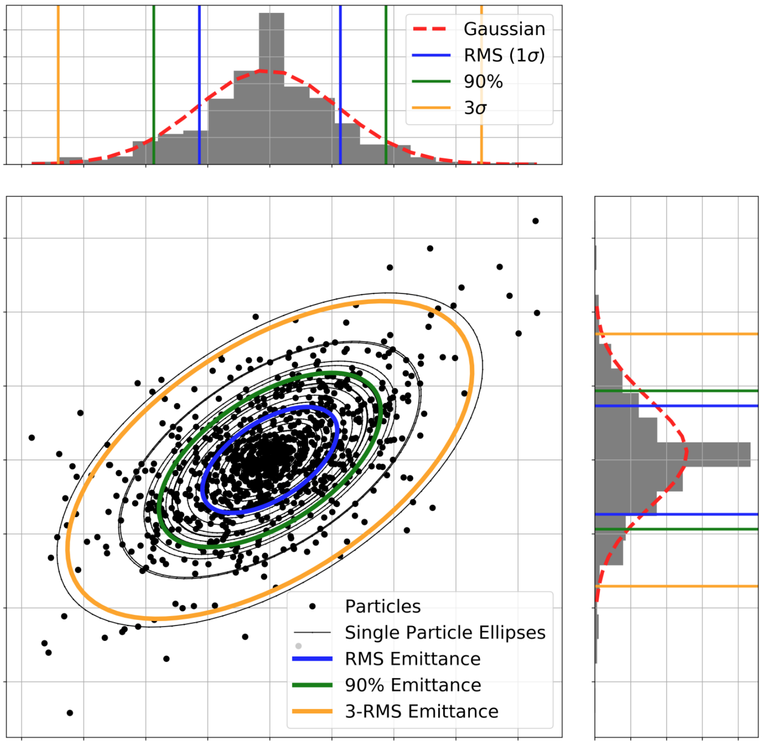

Figure 2.6: Transverse phase space of a bunch

and the RMS momentum spread in the vertical histogram with the two blue lines. The quantity:

$$\epsilon_{u,RMS} := \sqrt{det(\Sigma_{u,RMS})} \equiv \sqrt{< u^2 >< u'^2 > - < uu' >^2} \tag{2.30}$$

is defined as the RMS emittance or the geometric emittance of the bunch. The geometric emittance is related to the area of an ellipse: using the Twiss parameters and the Figure 2.5 one can draw an ellipse that occupies an area equal to $\pi \cdot \epsilon_{u,RMS}$ (blue ellipse on Figure 2.6). According to Liouville's [17] theorem the density in the phase space is constant if the particles are under the influence of conservative forces (i.e. no interaction between the particles).This makes the geometric emittance an invariant of the motion of the bunch, just like the action is the invariant of a single particle. By definition the Sigma matrix is related to the Beta matrix via the emittance:

$$\Sigma_{u,RMS}(s) = \epsilon_{u,RMS} B_u(s). \tag{2.31}$$

The definition of the emittance requires a choice for the limiting in the phase space of the bunch. This choice is related to some number of standard deviations of the beam distribution and it is just a convention: the 1-sigma or rms emittance (previous case), the 90 % emittance (green ellipse on Fig. 2.6), the 3-sigma emittance (yellow ellipse on Fig. 2.6), and so on. In this study only the RMS emittance will be used.

The geometric emittance is an invariant of the motion only if the energy of the beam is not changing: no electric field is present and no energy is being lost from the particles. In the case of acceleration the geometric emittance does not stay constant. For this reason, the normalized emittance is defined which is preserved during acceleration:

$$\epsilon_{u,n} := \beta_{rel}\gamma_{rel}\epsilon_u. \tag{2.32}$$

The units of the emittance are $m \cdot rad$ but most commonly are used the units $mm \cdot mrad$ or μm. The normalized transverse emittances in the PSB are in the range of $\epsilon_x = 1$ to 15 $mm \cdot mrad$ and $\epsilon_y = 1$ to 9 $mm \cdot mrad$ [9].

The emittance is an extremely important parameter for any accelerator. It defines the beam envelope and therefore plays a very important role in the definition of the physical aperture of the accelerator (acceptance). The acceptance will determine the size of the vacuum chamber.

The emittance is also a key parameter to many other quantities that describe the overall performance of an accelerator such as the Brightness or the Luminosity. For example the luminosity of the LHC is given by the formula:

$$L = \frac{N_b^2 n_b f_{rev} \gamma_r}{4\pi\epsilon_n \beta^*} F, \tag{2.33}$$

where N_b is the number of particles per bunch, n_b the number of bunches per beam, f_{rev} the revolution frequency, γ_r the relativistic gamma factor, ϵ_n the normalized transverse beam emittance, β^* the beta function at the collision point and F a geometric luminosity reduction factor due to the crossing angle at the interaction point. Also the brightness is defined as the intensity over the half-sum of the horizontal and transverse normalized emittances:

$$B = \frac{I}{\frac{1}{2}(\epsilon_x + \epsilon_y)}. \tag{2.34}$$

In the PSB for example the beams intended for the LHC physics runs are produced at a constant brightness [23].

2.4.4 Off-Momentum Particles - Dispersion

Everything that was discussed so far is for particles that have zero momentum offset or $\delta p/p = 0$. A realistic beam, however, is made of particles with a longitudinal momentum distributed around the synchronous momentum p_0. In the case of the PSB this is of the order of 0.1 %. Starting again from the Hill's equation and considering non-zero momentum spread, the differential equation of motion for the horizontal plane becomes inhomogeneous. This is because dipoles bend differently particles with different momenta. In this case the general solution can be represented as:

$$x(s) = x_b(s) + x_D(s) \equiv x_b(s) + D(s)\frac{\delta p}{p}, \tag{2.35}$$

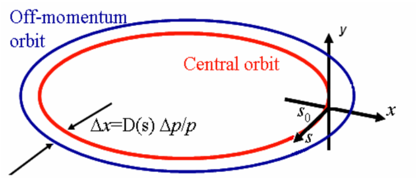

Figure 2.7: Closed orbit for non-zero dispersion

where $x_b(s)$ is the homogeneous solution, eq. (2.15), which describes the previous betatron oscillation and $x_D(s)$ is a partial solution of the inhomogeneous equation. The total motion of the particle is a betatron oscillation around the new closed orbit $x_D(s)$ that results from the momentum deviation of the particle (dispersion motion, Fig. 2.7). It is rewritten as the product of the dispersion function $D(s)$ and the momentum offset $\delta p/p$. The dispersion function expresses the linear correlation between the transverse position and momentum spread of the beam. By definition it satisfies the equation:

$$D(s)'' + K(s)D(s) = \frac{1}{\rho(s)}. \tag{2.36}$$

The dispersion represents the closed orbit of a particle with momentum offset of $\delta p/p = 1$. The analytical solution for the dispersion can be expressed as [22]:

$$D(s) = S(s)\int_0^s \frac{1}{\rho(s')}C(s')(s')ds' - C(s)\int_0^s \frac{1}{\rho(s')}S(s')ds', \tag{2.37}$$

where $C(s)$ and $S(s)$ are the elements of the general transfer matrix in eq. (2.27).

The dispersion contributes to the beam size of the bunch. The combined betatronic and dispersive motion has a result the growth of the horizontal phase space area that the beam occupies and therefore the increase of the beam size. If the beam distributions, the transverse and the longitudinal, are all Gaussian the beam size can be expressed by [20]:

$$\sigma_x = \sqrt{\epsilon_x \beta_x(s) + (D(s)\frac{\delta p}{p})^2}. \tag{2.38}$$

In general a beam distribution can be non-Gaussian. In the PSB for example the longitudinal (dispersive) distribution follows a parabolic shape rather than a Gaussian one. In this case, the resulting beam size can be expressed as the convolution between the betatronic and the dispersive distributions:

$$\sigma_x = \sigma_{betatronic} \otimes (D(s)\frac{\delta p}{p}) \equiv \sigma_{betatronic} \otimes \sigma_{dispersive}. \tag{2.39}$$

2.5 Longitudinal Beam Dynamics

In the previous chapter an introduction to the transverse beam dynamics inside the magnetic field of a periodic structure of dipoles and quadrupoles was presented. This chapter briefly discusses the motion of the particles in the longitudinal plane inside synchrotrons, focusing mainly in the definitions of the momentum compaction factor and the phase slippage factor that are later used in the dispersion measurement methods. A more detailed and mathematically solid description of the longitudinal beam dynamics can be found in [24, 25].

The longitudinal motion is mostly determined by the distribution of the electric fields inside the accelerator, since they act parallel to the velocity of the particles (eq. 2.1). In synchrotrons the energy and the momentum of the beams is modified using Radio-Frequency (RF) cavities. An RF cavity is a metallic chamber placed at a distinct place in the ring with two openings to allow the beams to pass through. In this chamber an alternating electric field is created along the particle path at a specific frequency f_{RF}. The energy gain ΔE of a particle inside a time-varying electric field is given by the expression:

$$\Delta E = e \int_{-g/2}^{g/2} \vec{E}(s, r, t) \cdot \vec{ds}, \tag{2.40}$$

where g is the distance in which the electric field is applied (cavity gap). The time-variant part of this field has a sinusoidal form with an angular frequency $\omega_{RF} = 2\pi f_{RF}$ while the spatial part is constant and equal to the applied voltage V_{RF} over the cavity gap:

$$\vec{E}(s, r, t) = \frac{V_{RF}}{g} \sin\left(\int_0^t \omega_{RF} dt + \phi_0\right), \tag{2.41}$$

where ϕ_0 it initial phase. This is a simplified model of the electric field produced inside the RF cavity which is valid for most cases of synchrotrons.

If a particle passes through the RF cavity when this alternating field is zero then it will remain unaffected. Otherwise it will gain (accelerate) or lose (decelerate) energy. In order to constantly accelerate the particles inside the synchrotron the particle must always arrive at the same amplitude of the electric field. This is achieved when the RF frequency is a multiple of the revolution frequency of the particle. The revolution frequency of a particle is defined as the ratio between its velocity over the total length of its trajectory:

$$f_{rev} = \frac{v}{C} = \frac{v}{2\pi R}. \tag{2.42}$$

Therefore the RF frequency is set to be:

$$f_{RF} = h f_{rev}. \tag{2.43}$$

This relation can be also expressed in terms of RF and revolution periods:

$$T_{rev} = h T_{RF}. \tag{2.44}$$

This condition is known as the synchronism condition. The parameter h is an integer called the harmonic number. The harmonic number specifies the number of bunches that a synchrotron can accelerate at the same time. For example, PSB can operate either in $h = 1$ or $h = 2$ [9]. From equation (2.43) it is obvious that the RF frequency must increase at the same rate as the revolution frequency.

As it was shown in the previous chapter, a particle with a small momentum offset $\delta p/p$ with respect to the nominal momentum of the reference particle will have a closed orbit C that has a different length from the nominal one. This change is expressed by the momentum compaction factor:

$$\alpha_p = \frac{dC/C}{dp/p}. \tag{2.45}$$

In most circular accelerators the momentum compaction factor is positive which means that higher momentum means longer circumference. But in some machines a negative momentum compaction factor can also be achieved [26]. In the PS Booster the momentum compaction factor is equal to 0.060934. It can be shown [25] that a_p depends on the lattice of the machine according to the relation:

$$\alpha_p = \frac{1}{C} \oint_C \frac{D_x(s)}{\rho(s)} ds, \tag{2.46}$$

where $D_x(s)$ is the dispersion function, $\rho(s)$ the bending radius and C the synchrotron circumference.

If a particle increases its energy (momentum) then its closed orbit will increase, for a positive momentum compaction factor. At the same time its velocity will also increase. The rate in which these two quantities change is not necessarily the same and therefore the behaviour of the revolution frequency is ambiguous. The evolution of the f_{rev} as the energy of the beam increases is described by the phase slippage factor. This factor is defined as the revolution frequency spread per unit of momentum spread:

$$\eta = \frac{df/f}{dp/p}. \tag{2.47}$$

If $\eta > 0$, then the revolution frequency increases while the energy (momentum) increases. On the other hand if $\eta < 0$ then the frequency decreases for a larger momentum of the particle. Combining equations (2.42) and (2.45) and using the definition of the relativistic momentum it is easy to show [25] that the slippage factor can be written as:

$$\eta = \frac{1}{\gamma^2} - \alpha_p, \tag{2.48}$$

where γ is the relativistic gamma factor of the particle. The energy that corresponds to $\eta = 0$ is defined as the transition energy. In this energy the increase of the velocity is exactly the same with the increase of the closed orbit trajectory. In this case the $\gamma-$factor is:

$$\gamma_{tr} = \sqrt{\frac{1}{\alpha_p}}, \tag{2.49}$$

and thus:

$$\eta = \frac{1}{\gamma^2} - \frac{1}{\gamma_{tr}^2} \tag{2.50}$$

From this equation is clear that at low energies $\eta > 0$ while at high energies $\eta < 0$. The PS Booster operates always below transition energy. Others accelerators, like Proton Synchrotron for example, cross the transition energy during their acceleration cycle.

The ideal (reference) particle that runs on the design orbit defined by the dipole magnets will arrive at the RF cavity with a phase of $\phi_s = \omega_{RF} t_s$ (Fig. 2.8 [25]). A particle that arrives later than the nominal (particle 1 of Fig. 2.8) will see a higher electric field which will increase its revolution frequency (if below transition) and move it towards the nominal one. Similarly a particle that arrives earlier than the nominal (particle 2 of Fig. 2.8) will see a smaller electric field which will decrease its revolution frequency. This results to an oscillation of the particles of a bunch around a central point (the reference particle) known as synchrotron oscillations. The frequency of these oscillations (synchrotron frequency) is usually small (scale of Hz or kHz). The maximum distance that particles can oscillate around the center without being lost from the bunch it defines the bucket size.

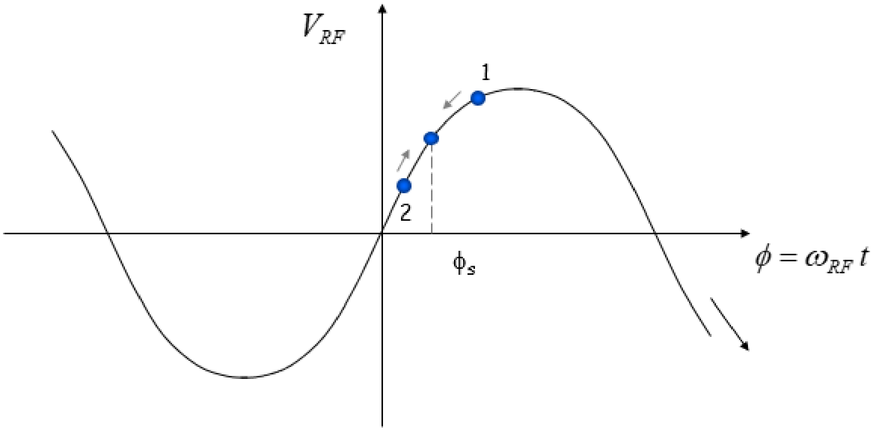

Figure 2.8: The principle of phase stability and synchrotron oscillations

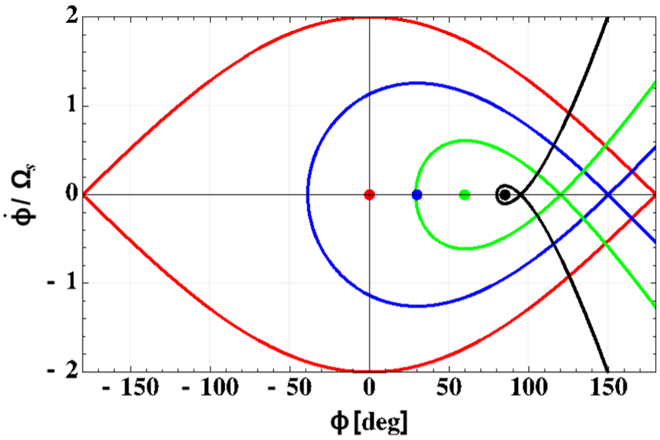

Figure 2.9: Longitudinal phase space below transition

Figure 2.9 shows the longitudinal phase space below transition for different values of the ϕ_s. The red line corresponds to $\phi_s = 0$ (no acceleration) where the size of the bucket becomes maximum. Particles inside the bucket will oscillate (rotate) around its central point (synchrotron oscillations) while those outside will get lost. The rotation of the particles that are positioned further away from the center (large amplitude oscillations) is non-linear. If $\phi_s > 0$ (acceleration) the bucket size becomes smaller and therefore less particles can be captured by the RF cavity.

The curve that separates the stable from the unstable region is called the separatrix. The area of the bucket defines the longitudinal acceptance of the RF system while the area that a bunch occupies in the longitudinal phase space is the longitudinal emittance with units of [eV · s]. The longitudinal emittance in the PSB range from 0.3 to 2.3 $eV \cdot s$ [9].

In this Figure the longitudinal position of the particles is represented with its phase. The phase is related with the s-parameter from eq. (2.5) via the harmonic number [25]:

$$\phi = -h\theta = -\frac{h}{R}s, \tag{2.51}$$

where θ is the azimuthal angle around the synchrotron. In the vertical axis the parameter $\dot{\phi}/\Omega_s$ is plotted which is proportional to the energy (momentum gain) according to the relation [25]:

$$\dot{\phi} = -\frac{\eta h c}{\beta_s E_s R_s}\Delta E, \tag{2.52}$$

where β_s, E_s and R_s the relativistic beta, energy and bending radius of the synchronous particle respectively, η the phase slip factor, h the harmonic number, c the speed of light and ΔE the energy offset of a particle.

Chapter 3

Emittance Reconstruction

3.1 Beam Instrumentation in the PSB

3.1.1 Transverse Beam Profiles

In the previous chapter the importance of the emittance in the description of the motion in an accelerator and its overall performance was discussed. The emittance is a quantity that cannot be measured directly but it has to be calculated from other measurable quantities. In this study, the emittance calculation is based on the measurement of the transverse beam profile.

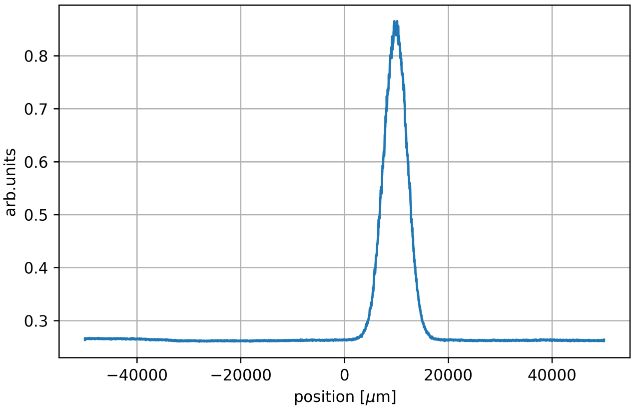

Figure 3.1: Transverse beam profile measured with the WS

In the rings of the PSB the transverse beam profile can be measured with the Wire Scanner (WS) [27, 28]. A WS consists of a thin carbon wire that crosses the beam during several turns. The wire speed is typically of the order of 10^{-15} ms^{-1}. The wire interacts with the charged particles through Coulomb scattering, creating a shower of secondary particles that are detected by two scintillators coupled to a photomultiplier. The photomultiplier creates an amplified current signal from which the transverse beam profile can be reconstructed. The WS is the baseline instrument to assess the PSB emittance. The scattering induced by the wire causes to the beam a measurable emittance "blow-up". A detailed analysis of this effect in the PSB at different energies can be found in [8]. Figure 3.1 shows a typical measurement of the transverse profile using the WS.

In order to derive the beam size from the bunch shape, a function is used to model the measured distribution. This function is employed to fit the data points of the profile using a non-linear least squares method [29]. The induced from the fit beam size error is taken into account in all cases. Typically the transverse bunch shape follows a normal (Gaussian) distribution:

$$f_G(x; A, \mu, \sigma) = \frac{A}{\sqrt{2\pi}\sigma} e^{-\frac{(x-\mu)^2}{2\sigma^2}}. \tag{3.1}$$

This function can be combined with a linear function in order to be able to include a non-zero baseline of the data points (5-parameters Gaussian function):

$$f_{5G}(x; c, m, A, \mu, \sigma) = c + mx + f_G(x; A, \mu, \sigma). \tag{3.2}$$

In many cases, however, the transverse profiles appear to have tails that differ from the ones of a normal distribution, especially for higher or lower than the operational intensities of the PSB. In order to model these tails a generalized Gaussian function was used (Q-Gaussian function [30, 31]):

$$f_{QG}(x; q, \beta, \mu) = \frac{\sqrt{\beta}}{C_q} e_q(-\beta(x-\mu)^2). \tag{3.3}$$

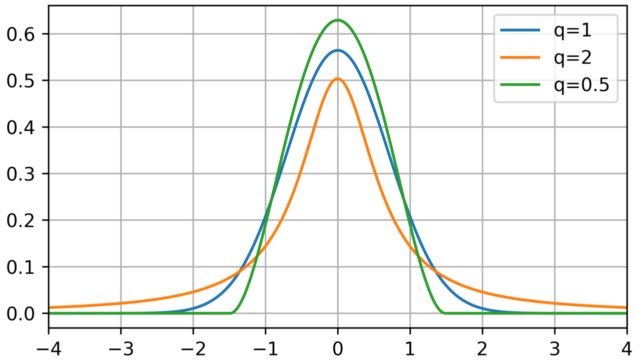

Figure 3.2: Q-Gaussian function examples

The parameter q describes the weight of the tails. For $q = 1$ the Q-Gaussian is identical to a Gaussian distribution. If $1 < q < 3$ the tails are heavier (overpopulated) than the ones of a normal distribution while for $q < 1$ are lighter (underpopulated). For example, if $q = 0$ the Q-Gaussian distribution is comparable to a parabolic function. Detailed expressions for the C_q and e_q functions can be found in [30, 32]. Figure 3.2 shows typical Q-Gaussian functions for different values of the q parameter. The RMS beam size in the Q-Gaussian function is calculated using the formula [32]:

$$\sigma = \frac{1}{\sqrt{\beta(5-3q)}}, \tag{3.4}$$

as long as the q-value is smaller than 5/3 which in the regime that we are interested this is the case [33].

A different instrument is used to measure the beam profile in the extraction line of the PSB. In the BTM transfer line three Secondary Emission Monitor [7] (SEM) grids have been placed. A SEM grid consists of a grid of stationary wires in which the beam passes through. Interactions between the charged particles of the beam and the wires induce an emission of secondary electrons. These electrons create a current to the wire that is connected to an individual channel. The signal that is produced from all the wires allows the reconstruction of the transverse beam profile. The resolution depends on the number of wires covering the crossing beam and the distance between them. The minimum wire spacing available is around 300 μm [10]. Figure 3.3 shows a typical set of measurement with the three SEM grids of the BTM line.

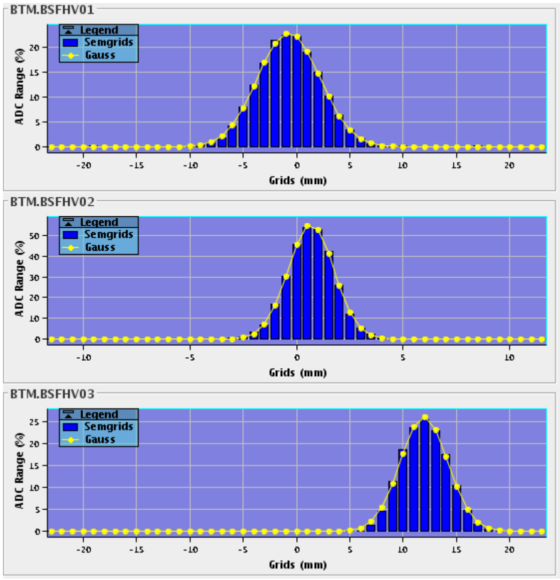

Figure 3.3: Transverse beam profiles measured with the three SEM grids of the BTM extraction line

3.1.2 Longitudinal Beam Profiles

The momentum spread of the beam can be determined from its longitudinal phase space distribution. The longitudinal phase space cannot be directly measured but it can be reconstructed using bunch profile data over many turns. In the PSB this is achieved through the Tomoscope application [34].

The measurement of the two dimensional longitudinal phase space is based on the principle of tomography which states that any two dimensional object can be reconstructed using all of its one dimensional projections [35]. At each turn, the particles inside the bunch rotate in the phase space due to the synchrotron motion, as it was described in Chapter 2.5. Snapshots of the longitudinal bunch profiles over a range of turns correspond to different projections of the phase space at slightly different angles. These profiles can be combined to recreate a first approximation of the initial two dimensional distribution. A set of bunch profile shapes can be also obtained from back projecting this first approximation, which are then compared to the initial ones. This yields to an iterative process which converges to the unknown longitudinal phase space distribution. Considerable improvements of this algorithm have been made over the years by employing particle tracking and considering the non-linearity of large-amplitude synchrotron motion [36].

Figure 3.4 (left) shows 80 bunch profiles measured every 40 turns over a time span of 1.8 ms for a modified BCMS-type beam of PSB ring 3. In the same figure (right) is shown the output of the Tomoscope application at extraction energy of the PSB. The colorbar expresses the density of the particles in the longitudinal phase space and the two horizontal and vertical profiles are the projection in time and energy of the distribution. In the longitudinal plane the PSB beams follow a parabolic distribution rather than a Gaussian one (Fig. 3.4). For this reason the RMS momentum spread is calculated using the second order moment formula (eq. 2.29).

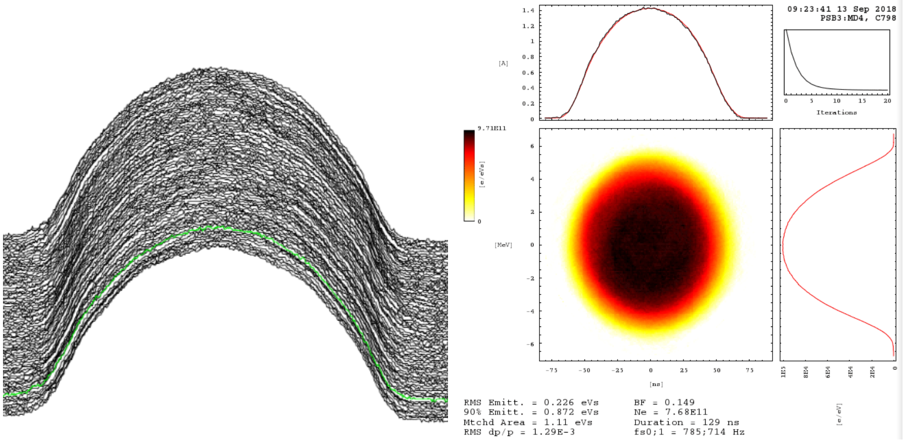

Figure 3.4: Bunch profiles (left) and reconstructed longitudinal phase space (right) from the Tomoscope application

3.1.3 Beam Intensity

Relevant to the brightness of the beam is the intensity (eq. 2.34) which is the amount of particles delivered at a certain energy. In the PSB the intensity is determined using the Beam Current Transformers (BCTs) [37]. PSB is equipped with different BCTs in the four rings but also in the BT and BTM transfer lines. A BCT measures the beam intensity by measuring the beam current through its magnetic field. The beam current is defined as:

$$I_b = \frac{qeN_p}{l}\beta c, \tag{3.5}$$

where N_p is the number of particles, e is the elementary charge and q is the charge state per unit of length l and velocity $v = \beta c$. BCTs operate in a limited frequency range that does not exceed the few hundreds of MHz which, for the PSB, is sufficient since the revolution frequency of its beams is less than 2 MHz. A detailed explanation for their working principle and the signal processing can be found in [38].

The Wall Current Monitor is a similar device that measures the instantaneous value of the beam current by measuring the voltage over a resistor that is put along a gap in the beam pipe [39]. Figure 3.5 shows a typical example of a WCM signal. The WCM together with a digital oscilloscope are the hardware that provide the input signals (the longitudinal bunch profile of the beam) to the Tomoscope application.

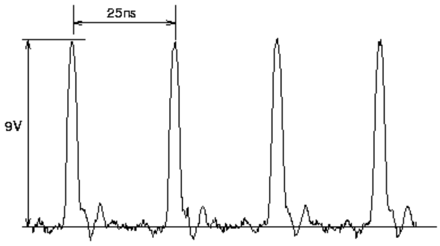

Figure 3.5: Output signal of a WCM measuring four bunches spaced at 25 ns intervals

3.2 Emittance Deconvolution

In the PSB, for the operational beams, the momentum spread is of the order of 0.1 % while the dispersion in the rings has an absolute value of around 1.5 m (Fig. 2.4). As it was discussed in Chapter 2.4.4 when the dispersion is non-zero and for a beam with non-zero momentum spread, the beam size becomes larger by a factor of $D\frac{\delta p}{p}$. Therefore in order to calculate the emittance, the dispersive part must be removed from the measured beam size. This removal is not trivial and there can be used different approaches to this problem. In this study two methods will be discussed:

- **Standard Gaussian Subtraction (SG)**
- **Full Deconvolution (FD)**

The first method holds the assumption that all the profiles (the measured, the betatronic and the dispersive) are Gaussian. In this case the relation between the three beam sizes is simplified to (eq. 2.38) (trivial deconvolution):

$$\sigma^2_{measured} = \sigma^2_{betatronic} + \sigma^2_{dispersive} = \sigma^2_{betatronic} + (D\frac{dp}{p})^2. \tag{3.6}$$

Solving for the betatronic beam size, one has:

$$\sigma_{betatronic} = \sqrt{\sigma^2_{measured} - (D\frac{dp}{p})^2}, \tag{3.7}$$

and therefore the normalized emittance is:

$$\epsilon_n = \beta_{rel}\gamma_{rel}\epsilon_{rms} = \frac{\beta_{rel}\gamma_{rel}}{\beta_{Twiss}}(\sigma^2_{measured} - (D\frac{dp}{p})^2), \tag{3.8}$$

where ϵ_{rms} is the RMS geometric emittance, β_{twiss} is the Twiss beta function at the position of the measurement and β_{rel} and γ_{rel} are the relativistic factors of the beam. The error of the emittance can also be worked-out through this relation analytically. This method is quite fast and valid for many occasions but only as an approximation.

A non-Gaussian dispersive distribution, as in the PSB, will lead to a non-Gaussian measured distribution. In this case the problem of calculating the betatronic distribution is equivalent to the problem of the deconvolution between the measured and the dispersive distribution [40], as in general:

$$\sigma_{meas} = \sigma_{betatronic} \otimes \sigma_{dispersive}. \tag{3.9}$$

There are some methods (algorithms) to do this [41, 42]. In the one that was adapted in this study it is assumed that only the betatronic profile is Gaussian. In order to deconvolute, both the dispersive and measured distributions are centered and normalized. Then a least square problem is solved between the measured data points and the discrete convolution of the dispersive distribution with a single-parameter Gaussian function:

$$f_{Conv}(x_i) = \sum_{j=1}^{N_p} disp(k_j) e^{-\frac{(x_i-k_j)^2}{2\sigma_b^2}}. \tag{3.10}$$

where N_p is the number of the measured data points. This single-parameter σ_b is the uknown RMS betatronic beam size. The emittance is simply then:

$$\epsilon_n = \frac{\sigma_b^2}{\beta_{Twiss}} \beta_{rel}\gamma_{rel}. \tag{3.11}$$

3.3 3-SEM Method

An alternative method is used in the PSB for calculating the emittance, which has the advantage of not using the optics beta function. This method is called the 3-profiles or 3-grids method [7, 43]. Assuming that one has three beam monitors at three positions

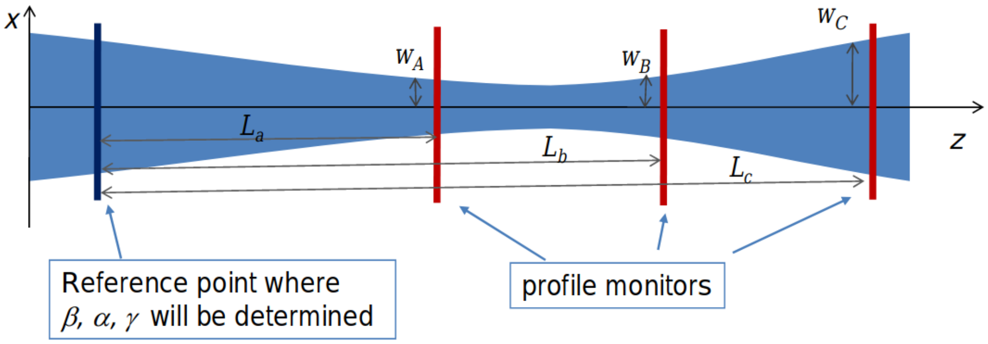

Figure 3.6: 3-SEM method

in a transfer line, that are separated with only drift spaces in between them (Fig. 3.6), it can be proven [43] that the betatronic beam sizes can be written as:

$$\begin{bmatrix}\sigma_1^2\\ \sigma_2^2\\ \sigma_3^2\end{bmatrix} = \begin{bmatrix}1 & -2L_a & L_a^2\\ 1 & -2L_b & L_b^2\\ 1 & -2L_c & L_c^2\end{bmatrix}\begin{bmatrix}\beta\epsilon_{rms}\\ \alpha\epsilon_{rms}\\ \gamma\epsilon_{rms}\end{bmatrix}, \tag{3.12}$$

where L_a, L_b and L_c the distances from the monitors of a reference point and α, β and γ optics functions at this point. Solving this linear system one can find the quantities $\beta\epsilon_{rms}$, $\alpha\epsilon_{rms}$, $\gamma\epsilon_{rms}$ and then the geometrical emittance (by definition) from the formula:

$$\epsilon_{rms} = \sqrt{(\beta\varepsilon_{rms})(\gamma\epsilon_{rms}) - (\alpha\epsilon_{rms})^2}. \tag{3.13}$$

Furthermore, the calculation of the Twiss parameters at the reference point is trivial:

$$\beta = \frac{\beta\varepsilon_{rms}}{\epsilon_{rms}}, \alpha = \frac{\alpha\varepsilon_{rms}}{\epsilon_{rms}} \quad \gamma = \frac{\gamma\varepsilon_{rms}}{\epsilon_{rms}}. \tag{3.14}$$

This method is adapted to calculate the emittance in the BTM transfer line using the three SEM grids which are separated with only drift spaces. The reference point was assumed to be the first SEM grid, therefore $L_a = 0$. In this case also a deconvolution algorithm (SG or FD) has to be used in order to obtain the three betatronic beam sizes σ_1, σ_2 and σ_3.

The distances between the SEM grids is 2.5 m according to the layout of the BTM line. These distances have been corrected according to the survey measurements (with respect to the first grid):

$$\begin{aligned} L_b &= 248.5\,\text{cm},\\ L_c &= L_b + 248.7\,\text{cm} = 497.2\,\text{cm}, \end{aligned} \tag{3.15}$$

Figure 3.7 shows the error on the emittance, calculated with the 3-SEM method, as a function of the position error of the three SEM Grids, for a range of ±10 cm. The emittance is more sensitive on the position of the third grid in which, in the extreme case of +10 cm or −10 cm the error stays below 4 %. For the second grid the emittance error is asymmetrical for positive and negative displacements and the slope of the curve is opposite to the one of the third grid. The emittance error varies between +2 % and −4 %. The impact of the position of the first grid is minimal (errors of less than 1 %).

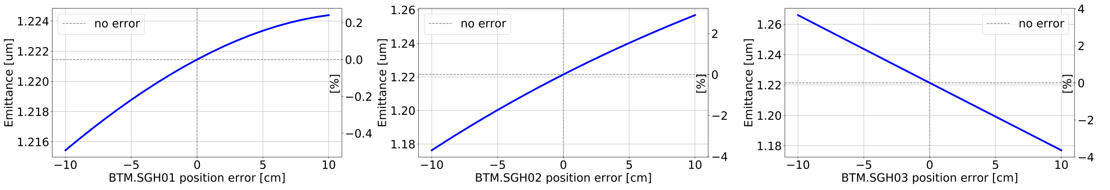

Figure 3.7: Emittance sensitivity on the positions of the SEM grids

The 3-SEM method is more unstable for small errors on the initial betatronic beam sizes. Figure 3.8 shows similar plots as the previous, but now the varied parameters are the beams sizes that are used as inputs in eq. (3.12). These parameters are varied by a ±10 % for a set of measurements close to the operational intensities ($75 \cdot 10^{10}$ ppb). The emittance error can be workout analytically using error propagation in eq. (3.13). Similarly as before the emittance is more sensitive to errors on the beam size of the third grid and less sensitive to errors of the first. The emittance errors can increase up to +10 % or −10 % which is can not be considered as negligible.

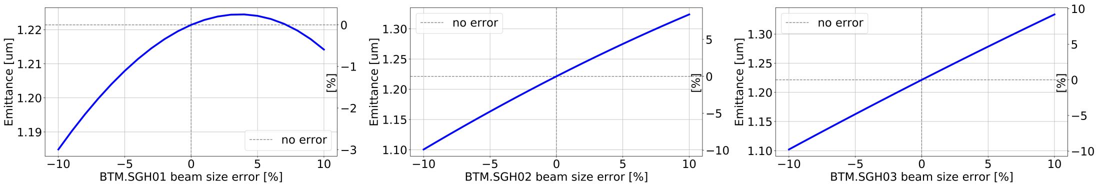

Figure 3.8: Emittance sensitivity on the betatronic beam sizes

Chapter 4

Impact of Systematic Errors

4.1 PSB-PS Emittance Discrepancy

The current injector capabilities do not allow the delivery of beams to the LHC that are within the HL-LHC project requirements. For this reason the injector chain, including PS Booster, will go through major upgrades as a part of the LIU project in order to increase the intensity and the brightness of the delivered beams. Two different beam types are mainly used in the LHC for the physics runs [44]: the nominal 25 ns beam ("standard" LHC25 beam) and a high brightness version of this, the Batch Compression bunch Merging and Splitting (BCMS) 25 ns beam. The achieved and the LIU target parameters of these beams at the extraction of the PS Booster are reported in the Table 4.1 [16].

PSB LIU requirements					
Status	Beam Type	I ($10^{11}p$)	$\epsilon_{x,y}$ (μm)	E (GeV)	$\delta p/p$ (10^{-3})
Achived	Standard	16.48	2.25	1.4	0.9
	BCMS	8.05	1.20	1.4	0.8
LIU target	Standard	32.50	1.80	2.0	1.5
	BCMS	16.25	1.43	2.0	1.1

Table 4.1: Beam parameters at the extraction of the PS Booster

The brightness of the beam is defined as the ratio between the intensity and the emittance of the bunch. In order to deliver the required high brightness beams to the LHC a tight budged in terms of emittance degradation was set. Previous studies [44, 45] showed that there is a considerable increase on the emittance between the PSB extraction and the PS injection. In particular, this emittance discrepancy is of the order of 40-50 % in the horizontal plane and about 15 % in the vertical plane for the nominal 25 ns beams. Similar is the case for the BCMS25 beams. Fig. 4.1 [46] shows the horizontal (left) and vertical (right) emittance along the accelerator chain for the years 2017 and 2018 (emittance taken from OP data without any special treatment).

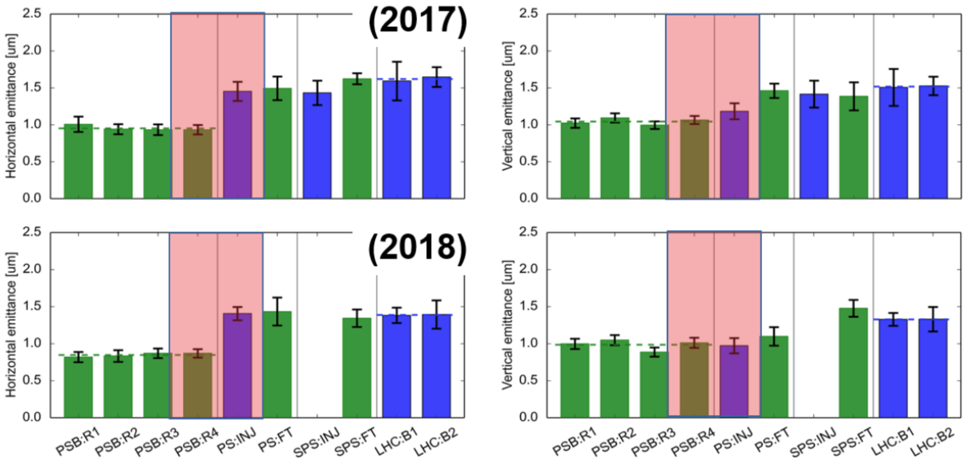

Figure 4.1: Emittance preservation along the accelerator complex

Part of this emittance discrepancy can be explained by the dispersion mismatch between the PSB extraction line and the PS injection that is present in the operationally used optics in the transfer line. Early studies in 2017 [47] showed that the emittance measured by the SEM Grids at the PSB BTM extraction line was also systematically larger than the emittance measured by the WS in the PSB rings for the BCMS beams, where there is no significant dispersion mismatch. This was observed for both planes and in all rings, with differences ranging from 5-20 %.

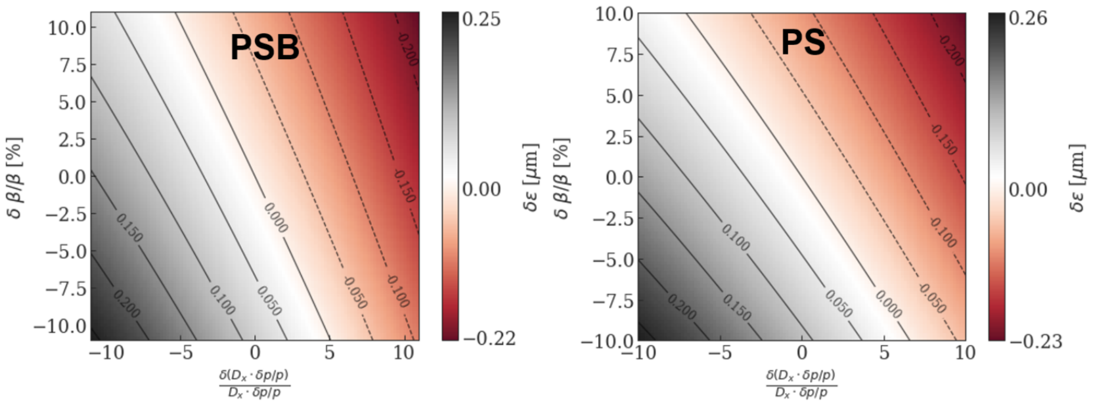

Figure 4.2: Emittance sensitivity on the optical parameters

As it was shown in Chapter 3, there is no direct way to measure the emittance in the PSB but it is derived through different reconstruction algorithms, using as input the transverse beam profile measurements and the machine optical parameters. In Figure 4.2, the emittance error has been analytically parameterized (eq. 3.8) and color-coded with respect to the error on beta function (horizontal axis) and the error on the dispersion (vertical axis), up to ±10 % [48]. The left plot corresponds to the PSB while the right one to the PS. It can be noticed that the emittance is very sensitive to the dispersion and the beta function. Systematic errors of these parameters can play a very important role on the final values of the emittance. This is especially important for the methods that are used in the horizontal plane, given the large dispersive contribution on the beam size, which, as it can be seen in the previous table, is expected to increase after the LIU upgrade. Limitations on the instruments that are used to measure the emittance (WS, SEM grids) can also be a source of errors [49] but these go beyond the scope of this study.

In this context and in the view of the LIU upgrade the precise and accurate measurement of the emittance is essential. For this reason systematic emittance measurements have been performed simultaneously in the PSB and in the PS using the operational BCMS25 beam and a modified BCMS beam with larger longitudinal distribution, for a range of intensities and with all the available instrumentation. The next chapters of this study will focus on the measurements that were carried out at the extraction of the PSB in order to:

- Explore and compare the brightness curves between the PSB WS and the SEM Grids of the BTM line for different beam characteristics.
- Understand the impact of systematic errors that are induced by the PSB optical parameters and the shape of the beam transverse distributions on the emittance calculation.
- Compare and optimize the emittance deconvolution algorithms (Standard Gaussian Subtraction and Full Deconvolution) and investigate their limitations and their behaviour under different conditions (intensities or beam types).

4.2 Measuring the Optical Parameters

The dispersion and the beta function are very important parameters for the emittance calculation, so their exact value has to be determined. Assuming Gaussian profiles (SG method), from equation (3.8), one can observe that the emittance depends quadratically on the dispersion:

$$\epsilon = \frac{\beta_{rel}\gamma_{rel}}{\beta_{twiss}}(\sigma^2_{measured} - (D\frac{dp}{p})^2). \tag{4.1}$$

Therefore a small error on the dispersion for example will induce an error twice as large on the emittance, for linear error propagation. In the Full Deconvolution method the resulting betatronic beam size, and therefore the resulting emittance, are also very sensitive to small errors on the dispersion. Under these conditions, a campaign to get as precise as possible values for the optical parameters was launched. In the next, the results of these measurements for the PS Booster will be presented and their impact on the brightness curves will be discussed. Similar measurements were also curried out for for the PS and are summarized in [50].

4.2.1 Dispersion Measurement in the PSB

The dispersion is defined as the dependence of the orbit change on the relative momentum offset:

$$D = \frac{dx_{co}}{d(\delta p/p)}, \tag{4.2}$$

where the x_{co} is the center (position) of the beam closed orbit and the $\delta p/p$ is the momentum offset of the beam. The constant term of this dependence is referred as the linear dispersion. The higher order terms define the higher order dispersions, such as the second order dispersion which depends linearly on $\delta p/p$ [51]. The dispersion is generated by dipoles and only propagated by quadrupoles. In an ideal machine the vertical linear dispersion is zero since the dipoles bend the beam only horizontally.

In order to experimentally determine the dispersion function, the closed orbit was measured for different values of $\delta p/p$. It is important to vary the beam momentum offset without changing the magnets configuration because this would destroy the optics and therefore the dispersion. This can be performed by introducing an energy offset to the beam. In the PSB this is realized by adjusting the frequency (BA.EXTREFFREQ) of the main RF system (C02), from its initial value $1,746,270$ Hz, to different values between an upper and a lower limit (changing the radial steering). In order to cover a large range of closed orbit values, a large range of frequencies was scanned.

Changing the RF frequency results to the change of the momentum spread according to equation (2.47):

$$\frac{\delta p}{p} = -\frac{1}{\eta}\frac{(f - f_{initial})}{f_{initial}}, \tag{4.3}$$

where f is the adjusted frequency value and η is the phase slip factor of the PSB. This factor is calculated using the relativistic parameters at extraction energy of the PSB:

$$\eta = \alpha_{c,PSB} - \tfrac{1}{\gamma_{extr}^2} \simeq -0.100081,$$

where $\alpha_{c,PSB} = \frac{1}{\gamma_{tr}^2} \simeq 0.060934$ is the momentum compaction factor of the PSB and $\gamma_{extr} = \frac{(1400+938.27)}{938.27} \simeq 2.492108$ is the gamma relativistic factor at 1.4 GeV energy. By sampling the response of the beam position as a function of the momentum offset the dispersion can be deduced. The beam position is measured with the Beam Position Monitor (BPM) [52]. BPMs are non-destructive beam diagnostics that provide information on the position of the beam in the vacuum chamber at the location of the monitor. In synchrotrons the BPMs are usually distributed around the ring in order to track and correct the beam trajectories.

In this study the dispersion was measured in all four rings of the PSB and in the BT-BTM transfer line in both planes at the positions of the BPMs (BRi.BPM, BT.BPM, BTM.BPM), the WS (BRi.BWS) and the three SEM Grids. The PSB has a BPM for each of the 16 periods of the 4 rings. In the second period there is also a Wire Scanner (WS). Therefore, for each ring, there are 16+1 positions where the dispersion can be measured and compared to the model. In order to calculate the mean beam position a

6σ 5-parameters Gaussian fit was applied to the bunch profiles of the WS and the SEM grids.

Figure 4.3 shows a typical set of x_{co} vs. $\delta p/p$ measurements using the WS of ring 3 in the horizontal plane. The slope of the applied linear fit is equal to the dispersion in meters. The dispersion in the vertical plane is close to zero as expected. The plot can be found in the appendix.

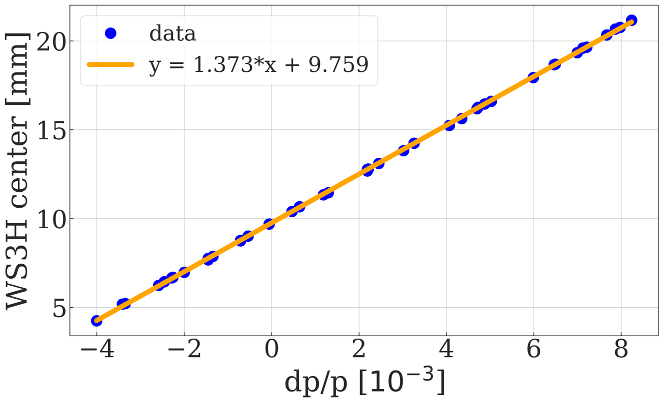

Figure 4.3: WSR3 horizontal measured dispersion

WS Dispersion (absolute values)				
Plane	Ring	Measured [m]	Model [m]	2017 values [m]
H	1	1.383 ± 0.014	1.4658	1.3619
	2	1.377 ± 0.023		1.3884
	3	1.3732 ± 0.0024		1.3634
	4	1.372 ± 0.014		1.3827
V	1	0.0874 ± 0.0027	0.0	0.0919
	2	0.0960 ± 0.0050		0.0114
	3	0.084 ± 0.011		0.0299
	4	0.0425 ± 0.0044		0.1101

Table 4.2: Measured dispersion at the WS of the PSB

The results are similar for the other PSB rings (1, 2 and 4). The plots can be found in the appendix. Table 4.2 summarizes the measured dispersion at the WS for all the rings and the comparison with the model. These values are very close, in most cases, with these measured in the previous year (2017 values) [49]. The uncertainty of the measured values corresponds to the error of the fit.

Following the same approach as with the WS, systematic dispersion measurements along the PSB rings were performed using all the BPMs around the machine. In the horizontal plane for all rings and for all BPMs the data points were very linear.Figure 4.4 shows the measured dispersion around the rings and it is compared with the model dispersion, as calculated by MAD-X [53], at extraction energy. In the upper plot of Fig. 4.4 the line represents the model, the dots the measured dispersion at the BPMs and the stars the measured dispersion at the WS. In the bottom plot of the same figure the relative differences between the model and the measured dispersion are shown.

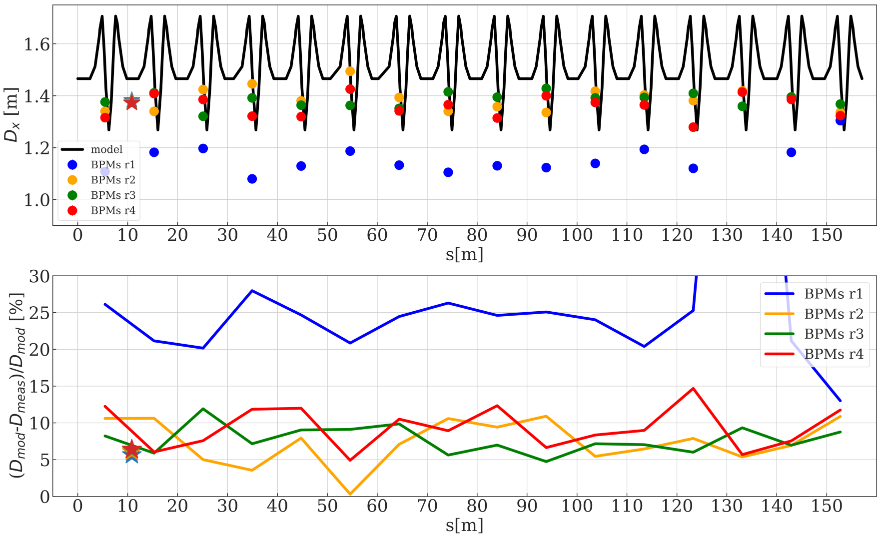

Figure 4.4: PSB Rings BPMs measured dispersion

The percentage differences between the measurement and the model ranges between 5 – 10 % for the BR2, BR3 and BR4 BPMs but it goes up to 20 – 30 % for the BR1 BPMs. Independent measurements were repeated for the BPMs of ring 1 but the results were the same: the dispersion that was measured is between 1.0 – 1.2 m and not between 1.3 – 1.4 m as of the other rings. Moreover, the data measured with the BR1.BPM14L3 were problematic and this data-point was thus removed from the plot. These measurements suggest that the calibration of the BPMs of ring 1 need to be revised by the Beam Instrumentation experts. For the WS the difference is around 5 %.

4.2.2 PSB BT-BTM Dispersion

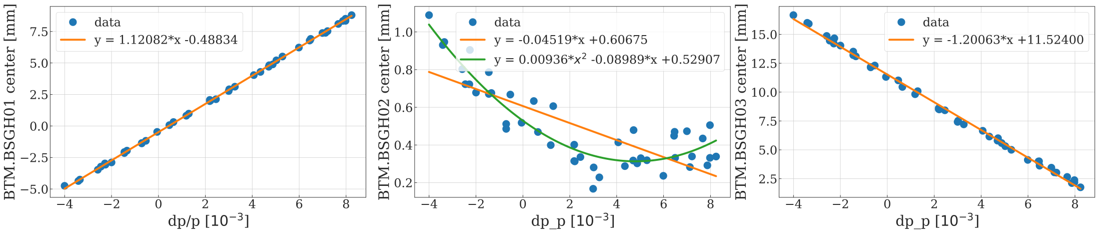

Figure 4.5: SEM Grids horizontal dispersion

The dispersion in the extraction line of the PSB was measured at the locations of the three SEM Grids (Fig. 1.5) and at the six BPMs (BT-BPM00, BT-BPM10, BT-BPM20, BTM-BPM30, BT-BPM40, BTM-BPM00, BTM-BPM10) of the BT-BTM transfer line, following the same procedure as described earlier. Typical plots can be seen in Figure 4.5. In the second grid the behavior is not linear anymore as at this location the linear dispersion is close to zero. A quadratic fit is more suitable in this case, as we start to be very sensitive to the second order dispersion term.

The vertical dispersion is non-zero in all cases. When the beam comes from different rings the optics, and therefore the dispersion, at the SEM Grids are not identical but have some small differences. Figure 4.6 shows the measured horizontal (top) and vertical (bottom) dispersion of the BT-BTM line. The lines represent the model dispersion, while the dots the measured dispersion at the BPMs and the stars the measured dispersion at the SEM grids.

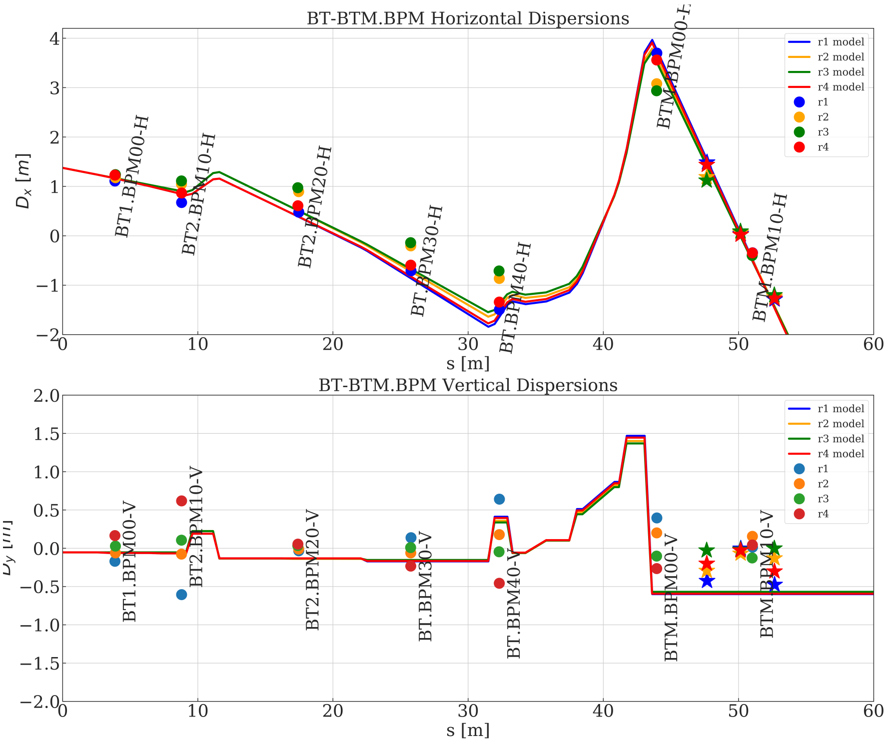

Figure 4.6: BT-BTM transfer line dispersion

The agreement between the model and the measured dispersion is satisfactory in most cases (especially for ring 1 and ring 4). The MAD-X files that were used to compute the model dispersion can be found in `https://gitlab.cern.ch/injector-optics/TransferLines/PSB-PS`. These optics functions are for protons at 2.12 GeV/c and the small horizontal dispersion optics (*_hor_emit_smallDx.str).

Table 4.3 summarizes all the measured values for the three grids in all rings and planes. The dispersion errors correspond to the errors of the linear (or quadratic) fits.

SEM Grids Measured Dispersion (absolute values)				
Plane	Ring	SEM01 [m]	SEM02 [m]	SEM03 [m]
H	1	1.4875 ± 0.047	0.037 ± 0.0010	1.289 ± 0.011
	2	1.1892 ± 0.029	0.0646 ± 0.0055	1.2298 ± 0.0097
	3	1.1208 ± 0.0032	0.0899 ± 0.0065	1.201 ± 0.010
	4	1.4434 ± 0.060	0.0215 ± 0.0071	1.268 ± 0.013
V	1	0.4252 ± 0.0052	0.0039 ± 0.0042	0.4757 ± 0.0076
	2	0.2936 ± 0.0017	0.0687 ± 0.0012	0.1305 ± 0.0049
	3	0.0276 ± 0.0017	0.0176 ± 0.0026	0.0019 ± 0.0049
	4	0.1998 ± 0.0009	0.0281 ± 0.0010	0.3019 ± 0.0022

Table 4.3: Measured dispersion at the SEM grids of the BTM transfer line

4.2.3 Beta-Function Measurement

In 2018 an extensive optics measurements campaign was performed for all rings of the PSB. This work was done by A. Garcia-Tabares, P.K. Skowroński and R. Tomás and is discussed in more details in [54]. As the knowledge of the beta-functions at the location of the WS is an important ingredient for the emittance computation, a summary of those measurements will be discussed in this section.

The accurate beta measurement in the PSB is a challenging task. It relies on the excitation of betatron oscillations in both the horizontal and the vertical plane using a kicker magnet. The excitation is applied either over a single turn or it is a continuous modulation close to the betatron frequency (AC Dipole). In these measurements the ACD excitation was mainly used. The dipole tune is defined as:

$$Q^D_{x,y} = \frac{f_{exc}}{f_{rev}}, \tag{4.4}$$

where f_{rev} is the revolution frequency of the beam.

Two methods were used for the reconstruction of the beta function. In the first method (N-BPM method [55]) the relative betatron phase between BPM pairs is derived from the harmonic analysis of the turn-by-turn (TbT) data. The phase advance is then used to calculate the beta functions according to the formula:

$$\beta^{\phi}(s_i) = \frac{\cot\phi_{ij} - \cot\phi_{ik}}{\cot\phi^m_{ij} - \cot\phi^m_{ik}}\beta^m(s_i), \tag{4.5}$$

where $\phi_{ij} = \phi(s_j) - \phi(s_i)$ are the measured phase advances between the BPMs j and i and the superscript m denotes the model values. The phase measurement is independent of BPM calibration and transverse misalignments. However, in the nominal optics of the PSB ($Q_x = 4.28$ and $Q_y = 4.30$ at injection) the phase advance between two consecutive

BPMs is very close to 90° causing large uncertainties to the measured values. This is due to the sensitivity of the β^{ϕ} to $\phi_{i,j}$ fluctuations near $\Delta\phi_{ij} = \pi/2$ [54].

The second method measures the amplitude of the betatron oscillations (eq. 2.15) [56]. The observed amplitude at the i^{th} BPM is modified according to its calibration factor C_i:

$$A_i = C_i\sqrt{\beta_{u,i}2J_u}. \tag{4.6}$$

The beta from amplitude can be calculated by using the formula [56]:

$$\beta_i^A = \frac{A_{u,i}^2}{2J_{u,i}}\frac{1 + r^2 + 2r\cos 2\pi\mu}{1 - r^2}, \tag{4.7}$$

with μ the betatron phase and r equal to:

$$r = \frac{\sin\pi(Q_d - Q)}{\sin\pi(Q_d + Q)}, \tag{4.8}$$

where Q_d is the ACD tune and Q is the natural beam tune. Smaller values of the tune difference:

$$\Delta Q_u = Q_u - Q_d \tag{4.9}$$

introduce larger excitation. The accuracy of the β^A is restricted by the precision of the BPM calibrations [54]. In order to overcome this limitation the beta function was measured in an alternative working point where the integer part of the tune was modified by on unit in both planes, going to an integer tune of 3 in the horizontal and 5 in the vertical plane. In this case the phase advance between the consecutive BPMs is not 90° anymore and the uncertainty of the β^{ϕ} is smaller. This uncertainty was minimized by optimizing the measurement parameters (beam intensity, distance between the driven and the beam tune ΔQ_u etc.). Then the β^{ϕ} values are used as a reference for the calibration. The nominal optics beta measurement is performed right after the calibration with similar beam conditions.

Figure 4.7 shows the beta from phase (β^{ϕ}), the beta from amplitude (β^A) and the beta from amplitude after the callibration ($\beta^{A,cal}$) for the nominal Q4Q4 optics as a function of the longitudinal position of the PSB. The WS of the PSB is positioned between the first and the second BPM. In order to propagate the beta function at the position of the WS the Twiss alpha function needs to be known. The alpha function is computed only by using the relative phases between the BPMs, which cause large error bars [54]. The relative beta error at the location of the PSB WS was estimated to be -10 ± 20 % with respect to the model value. Similar studies in the PS measured the beta function very close to the model with an error of less than 5 % [50, 57].

In the transfer line there is no need to measure the beta function for the emittance calculation since it is not used in the 3-SEM method. Table 4.4 summarizes the optical parameters at the position of the WS in the PSB and the PS alongside with the model values:

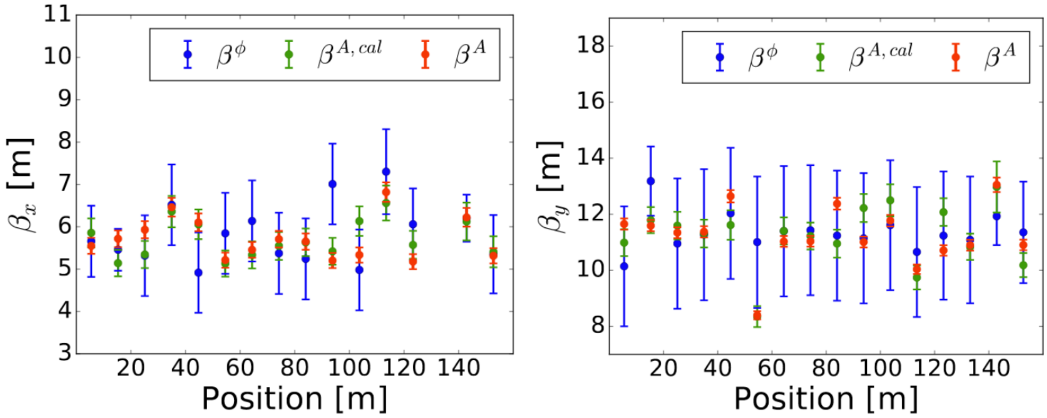

Figure 4.7: Horizontal (left) and vertical (right) measured β^{ϕ}, β^{A} and $\beta^{A,cal}$ functions for the Q4Q4 along the ring 1 of the PSB

WS Optical Parameters		
Parameter	PSB (BRi.BWS.2L1.H)	PS (PR.BWS.65.H)
β_x model	$5.7\ m$	$22.3\ m$
β_x measured	$5.1 \pm 1.0\ m$	$22.9 \pm 1.1\ m$
D_x model	$1.47\ m$	$3.17\ m$
D_x measured	$1.373 \pm 0.002\ m$	$3.17\ m$

Table 4.4: Model and measured optical parameters at the WS of the PSB and the PS

4.3 Brightness Curves at Extraction of the PSB

In this section the brightness curves at the extraction of the PSB using different instrumentation will be presented and compared with each other. The impact of the measured values of the optical parameters on the emittance calculation will be discussed. Measurements were performed in all 4 rings of the PSB.

The procedure for the emittance computation starting from a measured beam profile was described in detail in Chapter 3. In order to produce the brightness curves, systematic transverse beam profile measurements were acquired for different beam intensities, varying from 60-100E10 protons, using the BCMS25 beam setup.

Figure 4.8 shows the computed emittance versus intensity in the horizontal (left) and vertical (right) plane as measured with the SEM grids. The Simple Gaussian Subtraction was used for the dispersion subtraction and the emittance was computed based on the 3-SEM method. For the range of intensities from $60 \cdot 10^{10}$ *ppb* to $100 \cdot 10^{10}$ *ppb* the emittance varies from 0.8 to 1.6 μm, with a smaller spread in the vertical plane. This is due to the fact that in the vertical plane the dispersive contribution is negligible and therefore any error or fluctuation coming from the dispersion or the momentum spread of the beam has a small effect in the resulting emittance. Still in both planes this spread

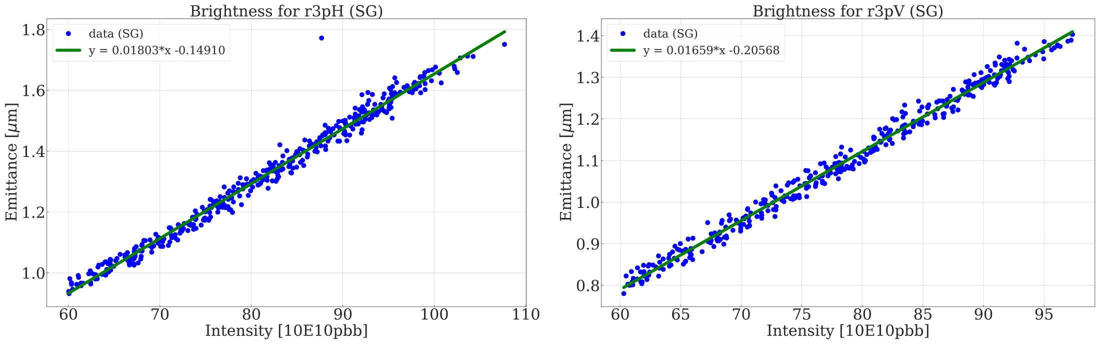

Figure 4.8: Brightness curves for SEM Grids

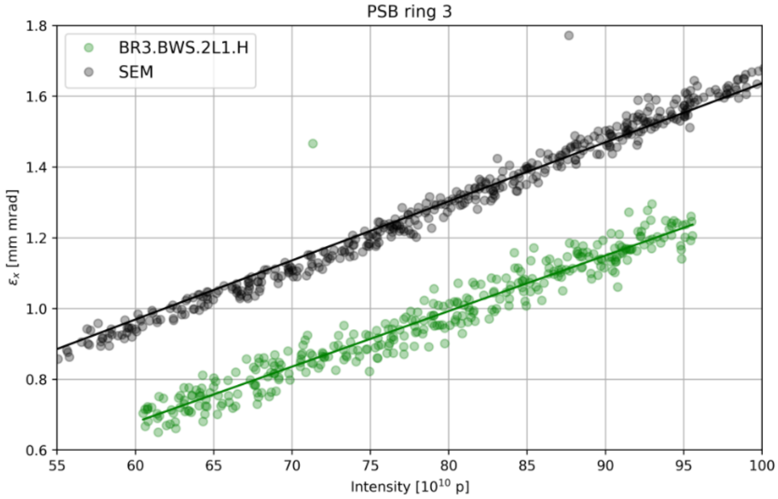

Figure 4.9: PSB R3 WS vs. SEM grids brightness curves with model optics

is non-negligible and it has been taken into account through the error of the applied linear fit (green line). These plots confirm the expected constant brightness of the PSB, which is by definition (eq. 2.34) proportional to the inverse value of the linear term coefficient. The results for the other three PSB rings are presented in the appendix. Small variations in the slope and in the offset of the linear fit are observed from ring to ring which are within the error of the fits.

Figure 4.9 shows a comparison of the measurements from the PSB ring 3 WS at extraction energy and the BTM SEM grids. One can notice that there is a significant inconsistency between the two brightness curves. The emittance at the extraction line is approximately 0.3 mm·mrad larger than the one inside the rings. The difference between the two instruments is comparable with these reported by previous studies [47]. No significant emittance difference is observed in the vertical plane (see appendix).

The emittance values of Figure 4.9 have been calculated using the model beta function and dispersion for both the ring of the PSB and the BTM line. Possible errors of these parameters can greatly affect the emittance values as it was demonstrated in Figure 4.2. In the previous chapter it was shown that especially in the position of the WS the difference between the measured and the model values are quite significant. At the position of the WS the dispersion was measured almost 7 % smaller and the beta function around 10 % smaller with a large uncertainty of 20 %.

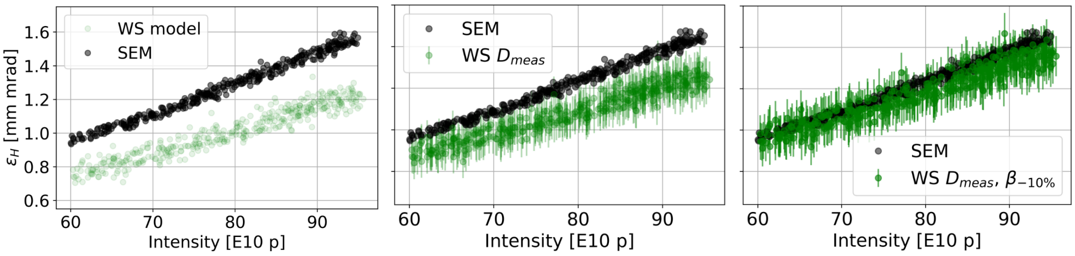

Figure 4.10: Left: brightness curves for the model dispersion and beta function. Center: applying the measured dispersion. Right: applying the measured beta function.

Figure 4.10 illustrates the impact of the measured parameters on the brightness of the WS. The left plot shows the emittance discrepancy when using the model optical parameters (Fig. 4.9). Applying the 7 % smaller measured dispersion the emittance gap becomes smaller in the middle plot of Figure 4.10. The errorbars correspond to the errors on the beam size and the dispersion. Finally in the right plot the measured beta together with its uncertainty has been used. The brightness of the WS matches the brightness of the SEM grids within the errorbars.

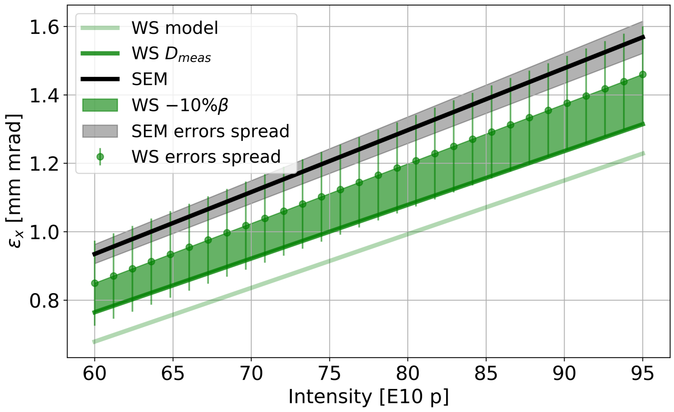

Figure 4.11: Impact of systematic errors on the brightness curves at the extraction of the PSB

Figure 4.11 summarizes the impact of the systematic errors on the brightness curves, plotting only the linear fits. A spread on the brightness of the SEM grids has also been added that includes the errors of the dispersion and the 3-SEM method. It is clear that the dependence of the brightness in the horizontal plane is strongly affected on the dispersion and beta errors. This gives a strong indication that the emittance discrepancy in operation is dominated by the systematic errors of the optical parameters. However, the large uncertainties in the measurement of the beta functions do not allow for solid conclusions.

It is worth mentioning that the momentum spread of the beam was reconstructed by tomography as it was described in Chapter 3.1.2. The $\delta p/p$ values that were used were taken directly from the Tomoscope application. The accuracy and precision evaluation of these values go beyond the scopes of this study.

4.4 Comparison with the Brightness Curves at the PS Injection

In parallel to the emittance measurements campaign at the extraction energy of the PSB, a systematic emittance measurement campaign was also performed at the injection energy of the PS. Figure 4.12 (left) shows the measured brightness curves at the injection energy of the PS (blue) and at the extraction energy of the PSB using the SEM grids (black) and the WS (green). In all cases the optical parameters of the model were used. The horizontal emittance discrepancy between the PSB and the PS as measured with the wire scanners in the two machines is of the order of 40-50%, in agreement with the observations during operation (see Fig. 4.1). The brightness measured by the SEM Grids lies between the other two curves.

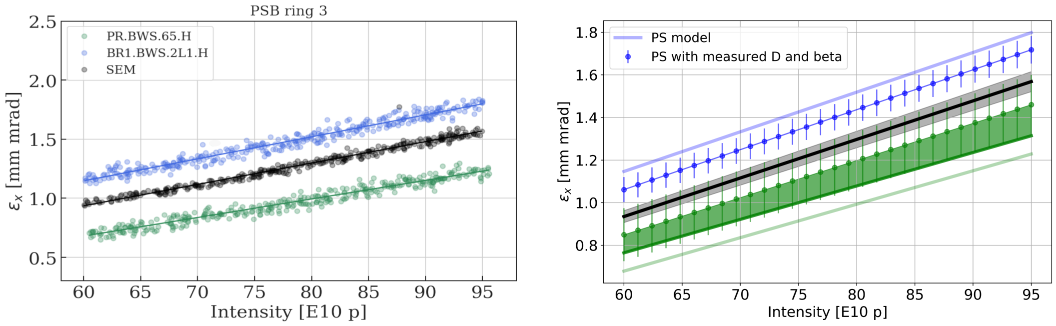

Figure 4.12: PSB-SEM-PS Brightness Curves for operational BCMS and the model optical parameters

In the operationally used optics of the BTP transfer line between the PSB and the PS, there is a known dispersion mismatch. The expected horizontal emittance blow-up due to this mismatch is around 0.15 mm·mrad [58, 59, 60] which is not sufficient to explain the large difference between the two machines.

Following the same procedure as for the PSB brightness curves, the PS brightness curves based on the measured optical functions were recomputed. In the case of the PS, however, the beta function measurement is much more precise than in the case of the PSB. The brightness curves of the PSB and the PS, using both the model and measured optical functions are summarized in Fig. 4.12 (right). It is interesting to notice that the difference between the PS bright curves using the measured optical functions and the PSB brightness curve as measured with the SEM Grids, is of the order of 0.15 mm·mrad, which agrees very well with the expected emittance blow up due to the dispersion mismatch in the transfer line.

Chapter 5

Errors Introduced by the Emittance Computation Algorithms

Having measured the transverse beam profiles one can determine the beam size by applying a fit to the data points using a mathematical function. The so far analysis is based on the assumption that these profiles follow a Gaussian distribution. In this chapter this assumption will be evaluated in order to quantify the impact of the distribution's shape on the calculation of the emittance and eventually on the brightness. Moreover, the errors that are induced by the emittance computation methods that rely upon this assumption will be estimated through a series of simulations.

5.1 Impact of Bunch Distribution on the Brightness Curve

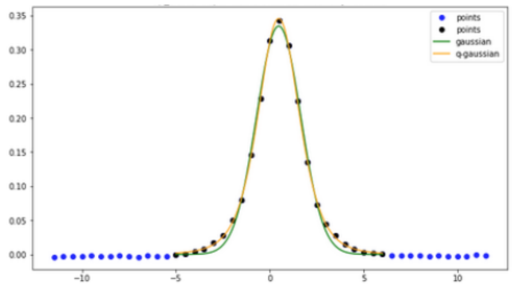

Figure 5.1: Measured transverse beam profile: Gaussian and Q-Gaussian fit

From the analysis of the transverse emittance versus intensity data that were presented in the previous chapter, it was observed that in many cases the bunch profiles follow non-Gaussian shapes. An example of a measured transverse beam distribution with the second SEM grid in the horizontal plane is shown in Figure 5.1. This distribution appears to have tails that differ from the ones of a Gaussian distribution. These tails can be modelled with a generalized version of a Gaussian function, the Q-Gaussian function, as it was demonstrated in Chapter 3. In this example two different fits have been applied: a Gaussian, which is represented by the green line, and a Q-Gaussian, which is represented by the orange line. The range of the data points used for the fit was limited to a few standard deviations (black points) because in some cases the baseline of the measured distribution would take negative values. Q-Gaussian fits were applied to all the data collected with both the SEM Grids and the WS, and the rms beam size was re-evaluated for each case.

To quantify the quality of the fit, the Relative Mean Square Error (RMSE) [61] was also computed both for the standard Gaussian and Q-Gaussian fits. The RMSE allows to qualitatively compute how concentrated are the data points around the fitted line. If y_i are the data points of the signal (the profile of the WS or the SEM Grids) and $y_{i,fit}$ are the values of the fit (at the positions of the data points), then the RMSE is given by the square root of the average squared residuals:

$$RMSE = \sqrt{\frac{1}{N_s}\sum_{i=1}^{N_s}(y_i - y_{i,fit})^2}, \tag{5.1}$$

where N_s is the number of samples of the signal. By dividing the RMSE with the mean value of the y_i values one gets the relative RMSE (rRMSE), which estimates the spread of the points around the fit:

$$rRMSE = \frac{RMSE}{\bar{y}} \cdot 100\%. \tag{5.2}$$

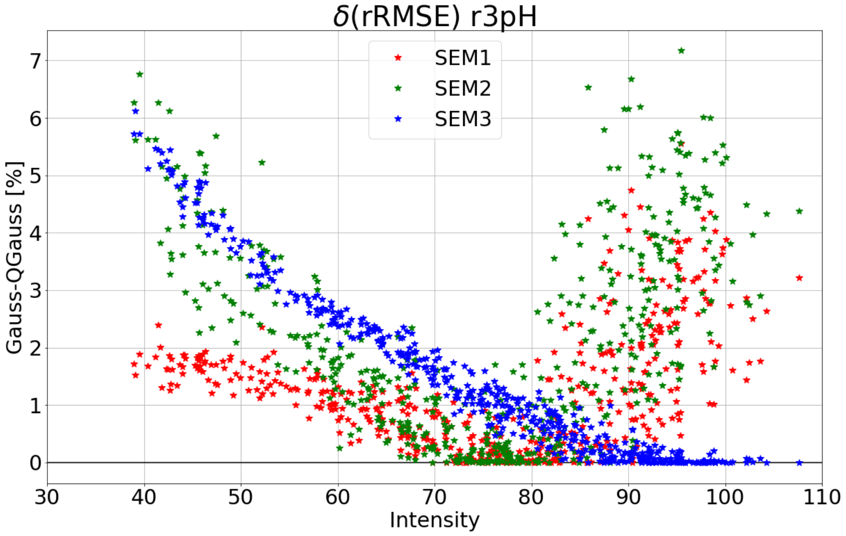

Figure 5.2: Gaussian and Q-Gaussian rRMSE

Figure 5.2 shows the difference between the rRMSE of the Gaussian and the Q-Gaussian fits of the profiles measured with the three SEM Grids, as a function of the intensity. The first observation that can be made is that in all cases the difference is positive. This means that the Q-Gaussian rRMSE is always less or equal to the one of the Gaussian, which indicates that it better models the bunch distribution. The second observation is that around the operational intensities ($75-85 \cdot 10^{10}$ ppb) the differences become minimum. This is less clear for the third grid where the minimum seems to be in higher intensities. For high (above $90 \cdot 10^{10}$ ppb) and low (less than $70 \cdot 10^{10}$ ppb) intensities the Q-Gaussian function seems to be a better choice for modelling the distribution.

Figure 5.3 shows the q-value as a function of the intensity for the three SEM Grids. For low intensities the q-value is less than one which corresponds to a distribution with underpopulated tails. For a q-value greater than one, which is the case for the high intensities, the tails are overpopulated. Close to operational intensities the q-value is approximately equal to 1 and the beam tails are identical to the tails of a Gaussian function. This is in agreement with the plot of Figure 5.2 in which the Gaussian function takes similar rRMSE values with the Q-Gaussian in the regime of the operational intensities.

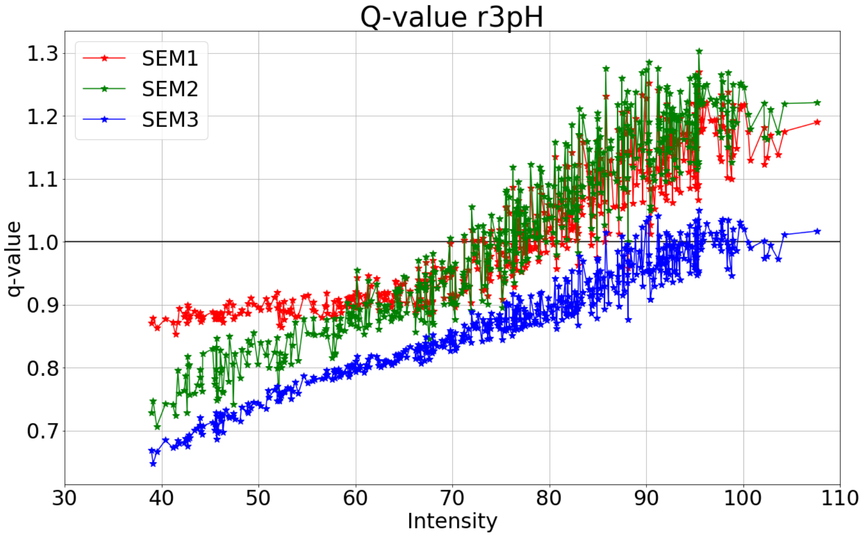

Figure 5.3: Q-Values for the three SEM Grids

In order to quantify the impact of the bunch tails in the brightness curves, the emittance must be recomputed using the new beam sizes of the Q-Gaussian fit as obtained from eq. (3.4). The q-values are always below 5/3 (Fig. 5.3). Figure 5.4 shows the brightness curves when assuming Gaussian (blue) and when q-Gaussian (red) distributions. It is clear that for low intensities the emittance was overestimated while for high intensities was underestimated. This is expected and it is consistent with the population of the distribution's tails (q-value). The overall effect is a change in the slope of around +50 %. The situation in the other rings is similar and can be found in the appendix (and also in [33]).

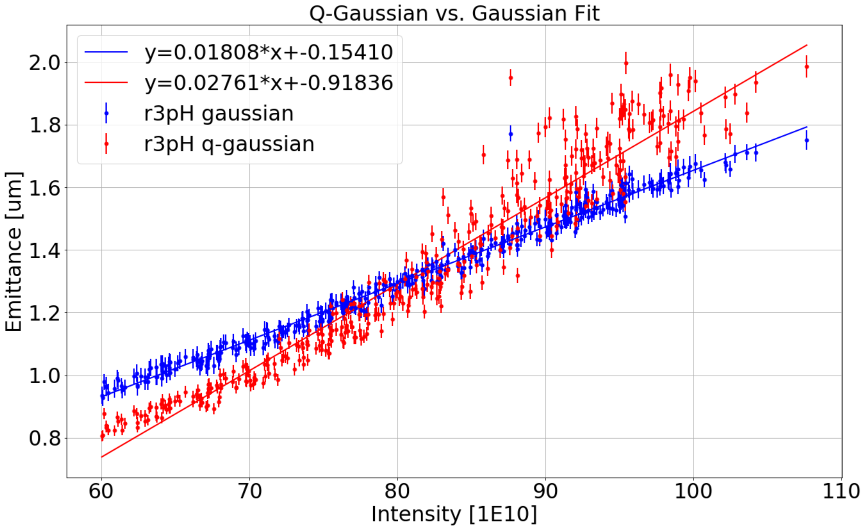

Figure 5.4: Impact of the shape of the bunch distribution on the brightness curve

5.2 Modeling Beam Distributions

The beam size of a bunch at a position with non-zero dispersion is the convolution between the betatronic and the dispersive beam distribution. As it was shown in the previous section the bunch distribution can have non-Gaussian tails that can greatly affect the brightness curve. Furthermore in the PS Booster the dispersive distribution of the LHC-beams follow a parabolic shape rather than a Gaussian one [62]. The subject of this section is to quantify the error introduced by the emittance computation algorithms on the emittance computation.

Figure 5.5 (left) shows a simulated Gaussian betatronic distribution, at a specific position inside an accelerator, with a defined emittance of 1.2 mm·mrad and a beta function of 5 m. These are typical parameters for the operational BCMS beam at the location of the BTM.SGH01, for intensities around $80 \cdot 10^{10}$ ppb (left plot of Fig. 4.8). The resulting betatronic beam size in this case is:

$$\sigma_{bet} = \sqrt{\epsilon_x \beta_x} = \sqrt{1.2 \cdot 5.0} \approx 2.45mm. \tag{5.3}$$

In a similar way a longitudinal (dispersive) distribution is simulated with defined RMS momentum spread of 0.1 % and a dispersion of $D_x = 1.5\ m$. The shape of this distribution is parabolic as the right plot of Figure 5.5 shows. For this distribution the "dispersive beam size" is equal to:

$$\sigma_{disp} = (\delta p/p)_{RMS} \cdot D_x = 1.5mm. \tag{5.4}$$

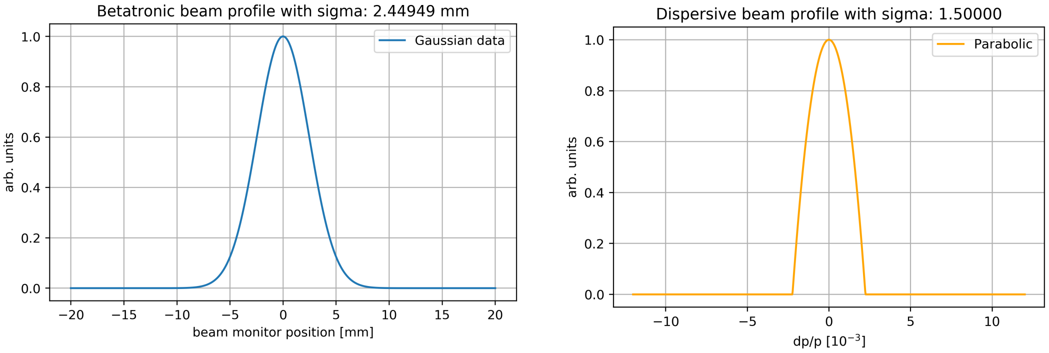

Figure 5.5: Simulated Gaussian betatronic distribution (left) and Parabolic dispersive distribution (right)

The distribution that an instrument will measure at this position is the convolution between the betatronic and the dispersive distributions. Because the dispersive distribution has a non-Gaussian shape the resulting measured is also expected to be non-Gaussian. Figure 5.6 shows the convolution on the left and the resulting measured profile on the right. As it can be seen from the applied fit a Gaussian function models the distribution with a good accuracy. This is because the dispersion contribution is relatively small: around 50 % smaller than the betatronic. Re-calculating the betatronic beam size with using only the measured and the dispersive distributions and the SG method, the resulting value is close to the initial defined one (eq. 5.3), with an error of 1.3 %.

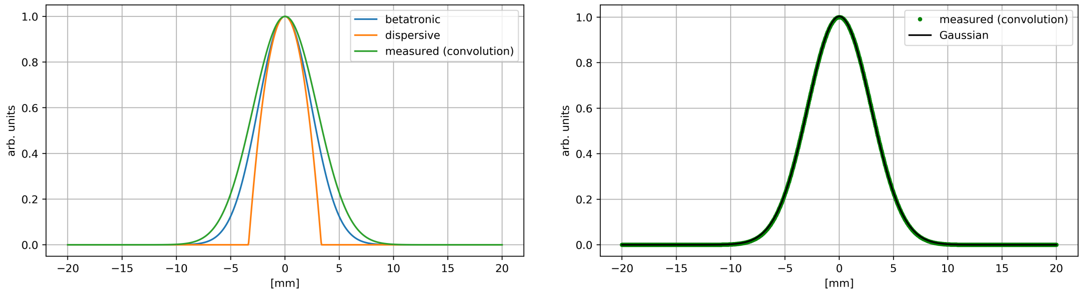

Figure 5.6: Convolution between a Gaussian and a Parabolic distribution

As the dispersive contribution becomes more significant the measured distribution becomes even more non-Gaussian and therefore the error of the SG becomes larger. This contribution can be expressed with the dispersive/betatronic beam size ratio. The ratio can be changed either by changing the intensity of the bunch or by changing the momentum spread of the beam. Figure 5.7 shows the relative betatronic beam size error of each method (SG and FD) as a function of the dispersive/betatronic ratio. It can be seen the error of the SG increases exponentially while the FD method has negligible errors.

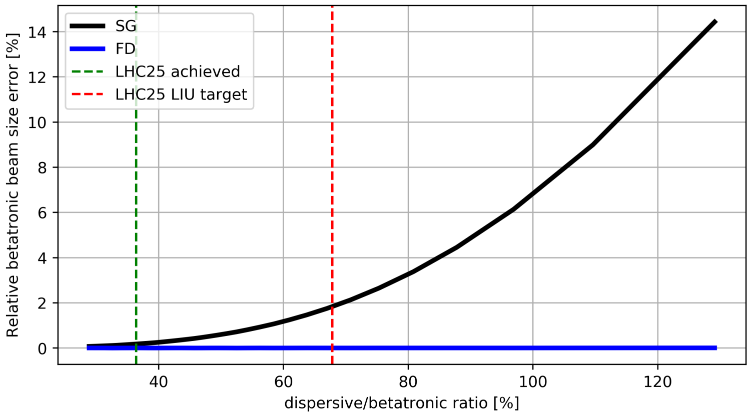

Figure 5.7: Betatronic beam size errors as a function of the dispersive contribution

From Table 4.1 and Table 4.4 one can determine the dispersive contribution at the position of the WS. For example for the standard 25 ns beam achieved parameters the ratio at the position of the WS is:

$$\begin{aligned} \sigma_{bet}^{ws} &= \sqrt{2.25 \cdot 5.1} \approx 3.39mm, \\ \sigma_{disp}^{ws} &= 0.9 \cdot 1.37 \approx 1.23mm, \\ \frac{\sigma_{disp}^{ws}}{\sigma_{bet}^{ws}} &= 36\%, \end{aligned} \tag{5.5}$$

which will lead to a negligible error on the betatronic beam size (green vertical line in Fig. 5.7). For the target LIU parameters, however, the dispersion distribution will become more significant. The ratio at the WS is expected to be in this case:

$$\begin{aligned} \sigma_{bet}^{ws} &= \sqrt{1.80 \cdot 5.1} \approx 3.03mm, \\ \sigma_{disp}^{ws} &= 1.5 \cdot 1.37 \approx 2.06mm, \\ \frac{\sigma_{disp}^{ws}}{\sigma_{bet}^{ws}} &= 68\%, \end{aligned} \tag{5.6}$$

in which the error on the betatronic beam size becomes around 2 % (red vertical line in Fig. 5.7).

But not only the dispersive distribution can have a non-Gaussian shape. From 5.3 it can be noticed that the q-parameter for high intensities can take values that are greater than one (overpopulated tails). The fact that the parabolic dispersive distribution corresponds to q-values close to zero (underpopulated tails) suggests that, in order to have $q > 1$, the betatronic distribution must also follow a non-Gaussian function. By changing the shape of the betatronic distribution the deformation of the measured profile becomes larger and starts to also have heavier or lighter tails, as Figure 5.8 shows.

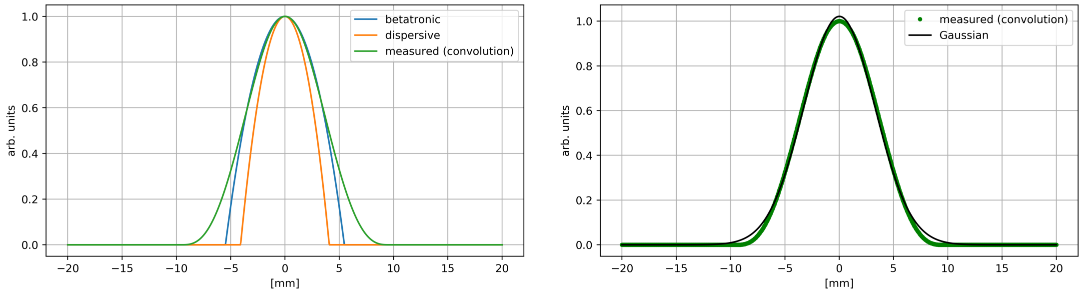

Figure 5.8: Convolution between a Q-Gaussian and a Parabolic distribution

In this case the errors of each deconvolution method behave differently. These errors are shown in Figure 5.9 and have been parameterized not only with the dispersive contribution but also with the q-value of a Q-Gaussian betatronic distribution. Scanning for a range of q-values between -0.7 and 1.4 the errors of the SG (left) and the FD (right) further increase. In these plots the vertical axis expresses the percentage error on the betatronic beam size with the sign corresponding to the overestimation (+) or the underestimation (-) of it. For example if $q > 1$ (heavy tails) and low dispersive/betatronic ratios (the betatronic is dominant) both methods underestimate the betatronic beam size. This is expected because the measured distribution has also heavy tails. The $q = 1$ lines correspond to the plot of Figure 5.7.

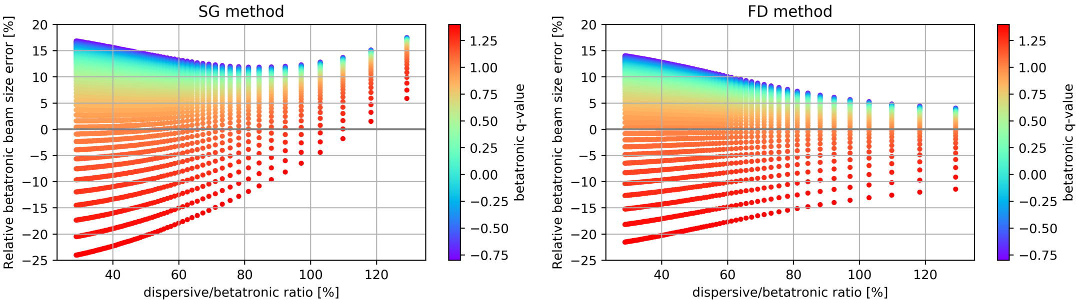

Figure 5.9: Betatronic beam size errors as a function of the dispersive contribution and the q-value

So far it has been discussed the error on the betatronic beam size. The error on the emittance, for the WS at least, can be found by using linear error propagation:

$$\begin{aligned} \epsilon &= \frac{\sigma_b^2}{\beta_{Twiss}}, \\ \frac{\delta\epsilon}{\epsilon} &= 2 \cdot \frac{\delta\sigma_b}{\sigma_b}. \end{aligned} \tag{5.7}$$

Therefore the emittance error is double the betatronic beam size error. For the LIU target parameters of the standard 25 ns beam this means an emittance error of 4 %. For the SEM Grids the calculation of the emittance error is more complicated to calculate since three beam sizes are used as inputs in the 3-SEM method and the emittance is the result of two quite complicated formulas (equations 3.12, 3.13). Sensitivity checks on the errors on the betatronic beam sizes of the 3-SEM method were presented in Figure 3.8.

5.3 Benchmarking Measurements

In order to test the predictions of the previous simulations using measured data an experiment was set up [63, 64]. A set of BCMS beam profile measurements took place at the ring 3 WS of the PSB for three different intensities, $55 \cdot 10^{10}$, $75 \cdot 10^{10}$ and $100 \cdot 10^{10}$ ppb, which correspond to different betatronic contributions and with different $\delta p/p$ values, corresponding to different dispersive contributions. The momentum spread of the beam was varied by changing the amplitude of the voltage of the C04 RF cavity, keeping constant the voltage of the C02 RF cavity. This way a longitudinal shaving of the beam is performed [9]. For each beam parameters the transverse profiles were measured with the WS while the longitudinal profiles with the Tomoscope application. Then the horizontal emittance was calculated using both the SG and FD methods.

Figure 5.10 shows the relative emittance differences between the two methods of calculation as a function of the momentum spread of the beam. The three colors correspond to the three different intensities. The two methods diverge when the contribution of the dispersive part of the profile becomes larger, i.e. for larger $\delta p/p$ and smaller intensities. Equivalent simulation studies in the PS arrive to similar conclusions [65]. Plotting the same data points not as a function of the momentum spread but as a function of the dispersive/betatronic ratio and comparing with the simulated differences of the two methods (Fig. 5.7) one can notice that there is a satisfactory agreement between the measurements and the simulations. The simulated curve has a small width because it includes a small range of q-values around $q = 1$. Similar were the results when using a different BCMS beam with larger momentum spread ($\delta p/p \approx 1.5 \cdot 10^{-3}$) [62].

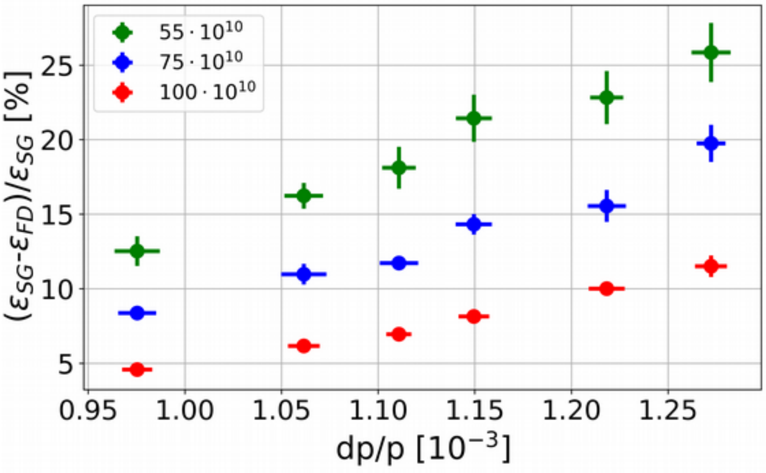

Figure 5.10: Relative emittance differences between the SG and FD methods

For lower ratios, and specifically close to the regime that the future LIU standard

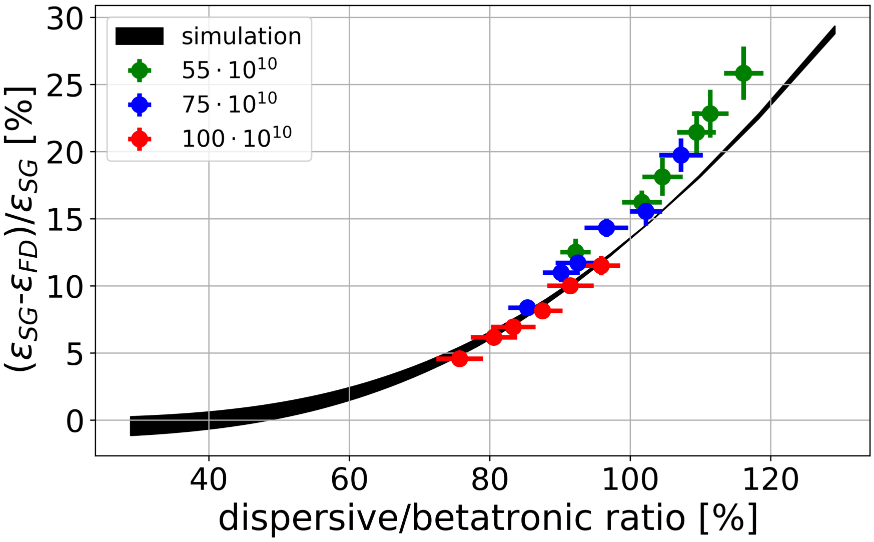

Figure 5.11: Benchmarking the measurements of the WS

LHC beams are expected to be (around 68 % as it was shown), the predicted relative errors coincide with the measurements within the uncertainty of the points. In general, this suggests that the FD method is more exact on the emittance computation. But the differences with the SG method are small, at least for the current standard LHC beam parameters (less than 36 %), and are expected to increase after the LIU.

For high ratios the data points start to diverge from the curve. A reason for this could be that is hard to know the exact dispersive/betatronic ratio of the experimental data points, since the betatronic beam size is unknown and it depends on the deconvolution algorithm. Furthermore, although the measured dispersive distribution follows a parabolic shape, in many cases it appears slightly deformed [62]. These small deformations can play an important role especially for the FD method which is very sensitive to the exact shape of the distribution.

Chapter 6

Summary

In the context of understanding the observed PSB-PS emittance discrepancy, systematic emittance measurements were performed at the extraction of the PSB Booster with all the available instrumentation and for different beam conditions. The goal was to understand the impact of the systematic errors on the brightness curves measured by the WS and the SEM grids. Possible sources of systematic errors are the optical parameters of the machine and the non-Gaussian shapes of the transverse beam distributions. Errors coming from the instrumentation were not part of this study.

The dispersion and the beta functions were measured for the four rings of the PSB and the BTM extraction line. Compared to the model, the measured dispersion and beta function at the location of the WS was found to be 7 % and 10 % smaller respectively. At the positions of the SEM grids the differences are relatively small. The emittance inconsistency between the two instruments is greatly reduced when applying the measured dispersion and beta function. However, the large uncertainties in the beta function measurement does not allow to come to solid conclusions.

A detailed study of the shape of the transverse bunch distributions at the extraction of the PSB revealed that the bunch tails appear to differ from those of a Gaussian function. This effect is more noticeable at low intensities (less than $70 \cdot 10^{1}0$ ppb) where the tails are underpopulated and at high intensities (greater than $90 \cdot 10^{1}0$ ppb) where the tails are overpopulated. These tails have been modelled with a Q-Gaussian function. The recalculated brightness results to a curve with a slightly different slope than the one that was previously calculated with the Gaussian function. The emittance at low intensities was overestimated while at high intensities it was underestimated.

The impact of the emittance computation methods on the emittance error was also estimated using simulated distributions. The non-Gaussian shape of the dispersive distribution in the PSB generates an increasing error to the Standard Gaussian (SG) method, as the dispersive contribution becomes larger. This is especially important for the future LIU beams where the dispersive contribution is expected to be almost twice as large. Possible non-Gaussian shapes of the betatronic distribution will further increase these errors for both SG and FD methods. A set of measurements were performed at the PSB in order to validate these predictions. A good agreement between the measurements and the simulations was shown.

Appendix A

PSB WS-SEM Dispersion

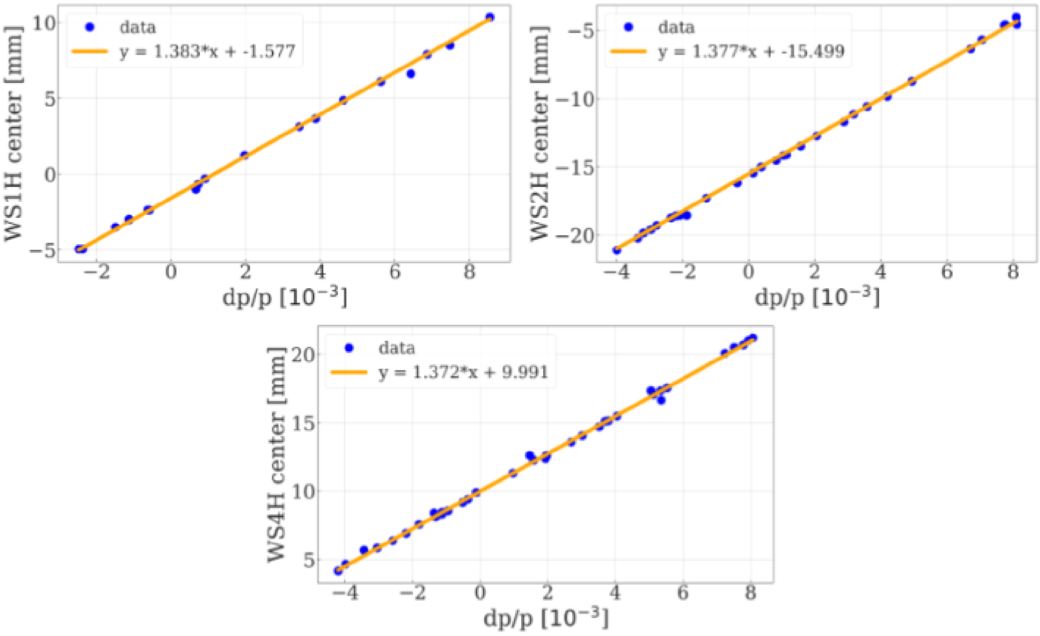

Figure A.1: R1H, R2H and R4H PSB WS measured dispersion

In the vertical plane the spread of the points is larger, in comparison to the horizontal plane, and a quadratic fit seems more suitable. This is because the linear dispersion is so small so that the second order dispersion emerges.

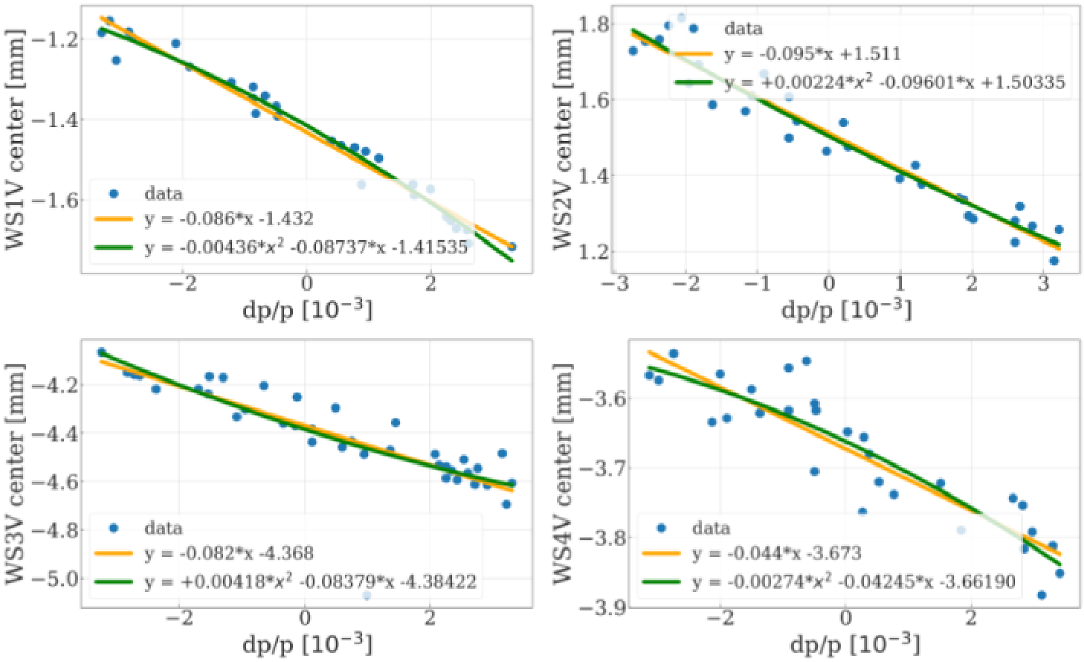

Figure A.2: R1V-R4V PSB WS measured dispersion

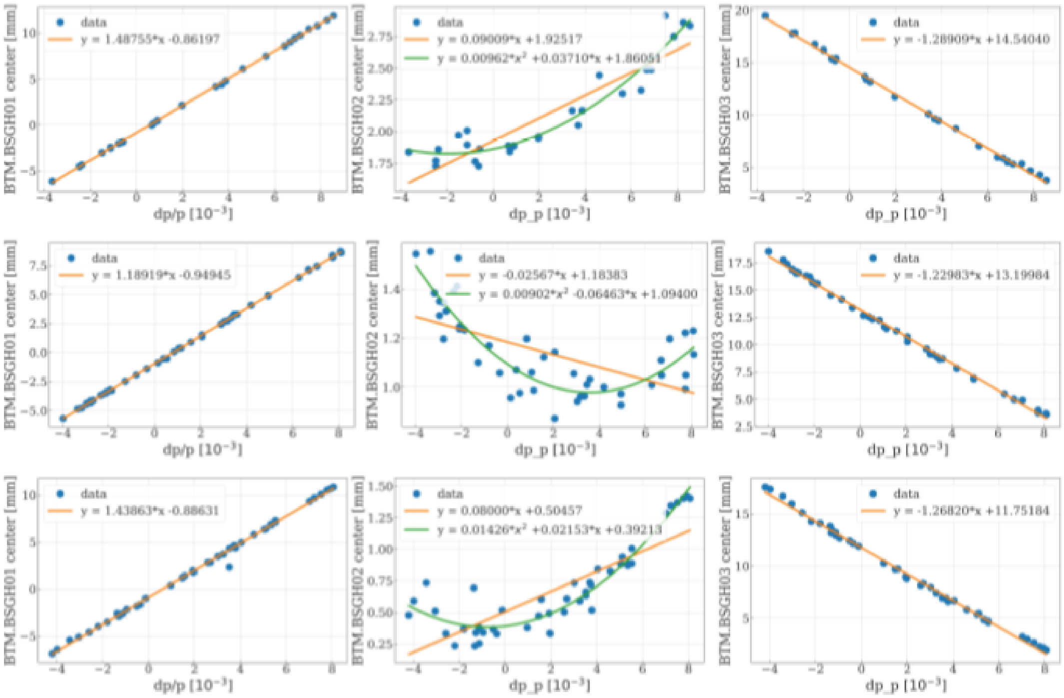

Figure A.3: R1H, R2H and R4H BTM SEM grids measured dispersion

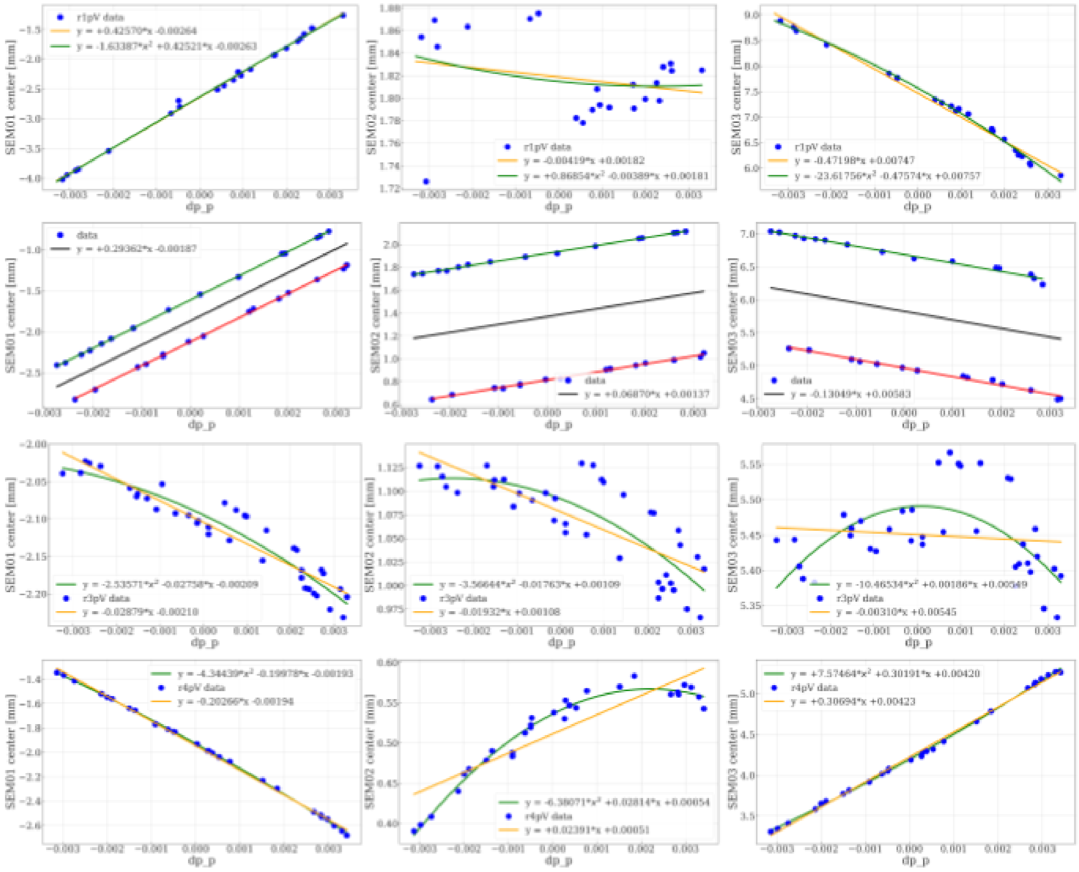

Figure A.4: R1V-R4V BTM SEM grids measured dispersion

Appendix B

PSB R1-R4 Brightness Curves

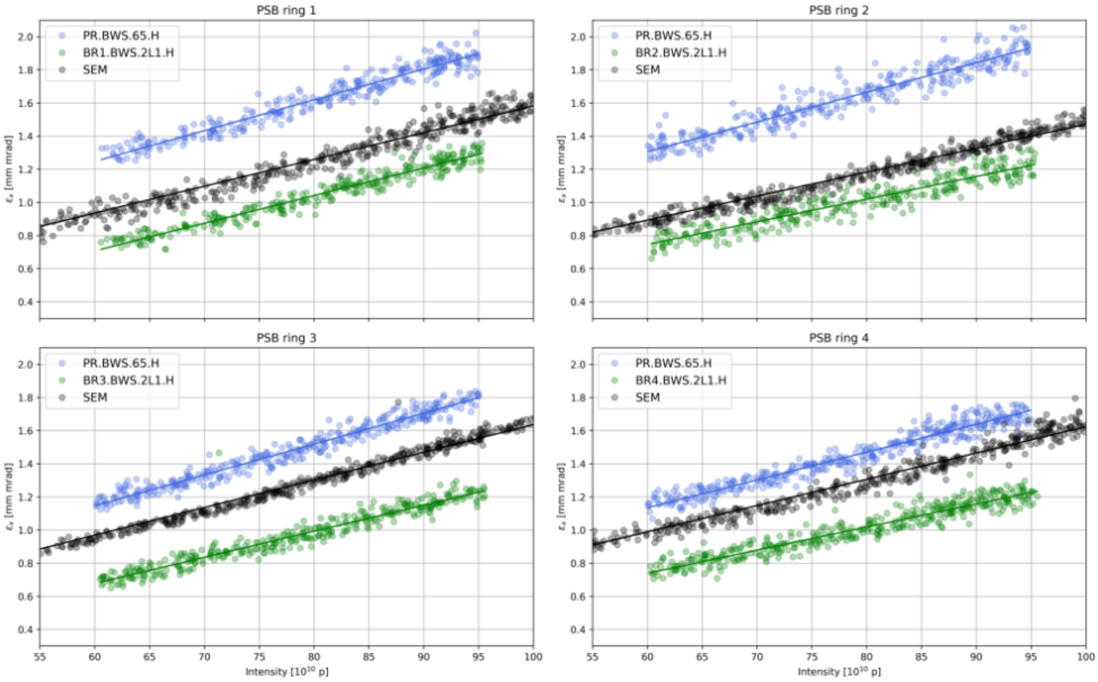

Figure B.1: PSB WS, SEM and PS horizontal brightness curves for all rings (SG method and model optics)

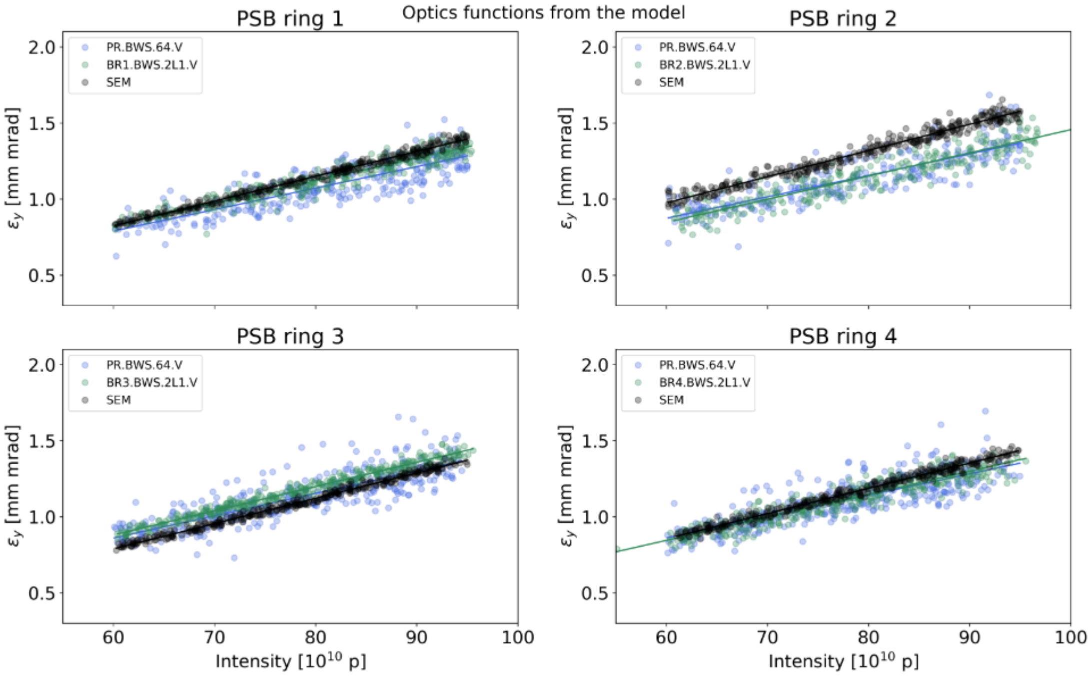

Figure B.2: PSB WS, SEM and PS vertical brightness curves for all rings (SG method and model optics)

Appendix C

Bunch Tail Effects in R1, R2 and R4 of the PSB

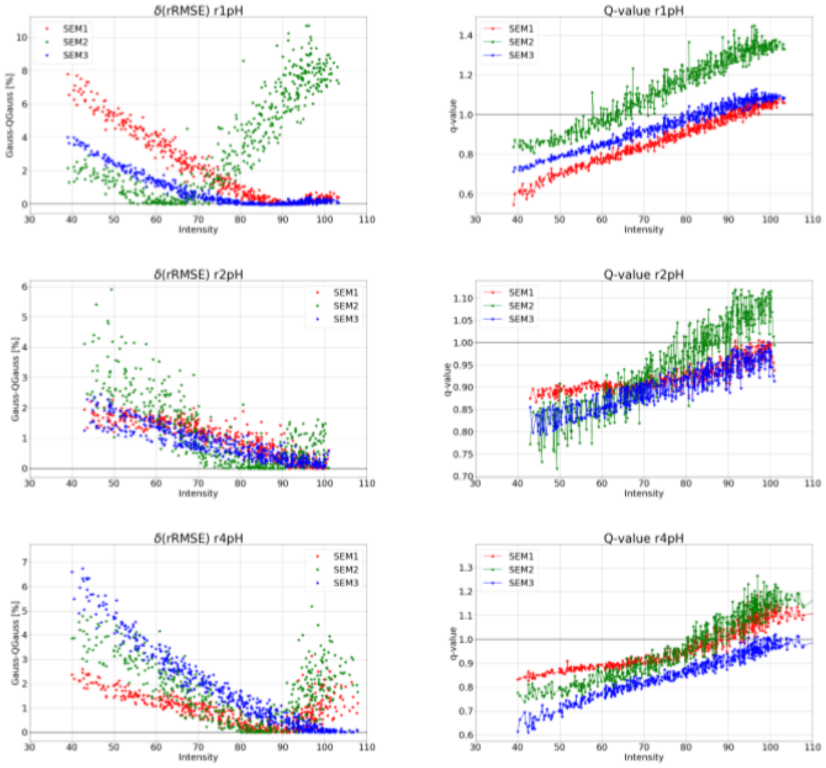

Figure C.1: Relative RMSE and q values of the transverse profiles measured by the SEM Grids when the beam is extracted from R1, R2 and R4 of the PSB

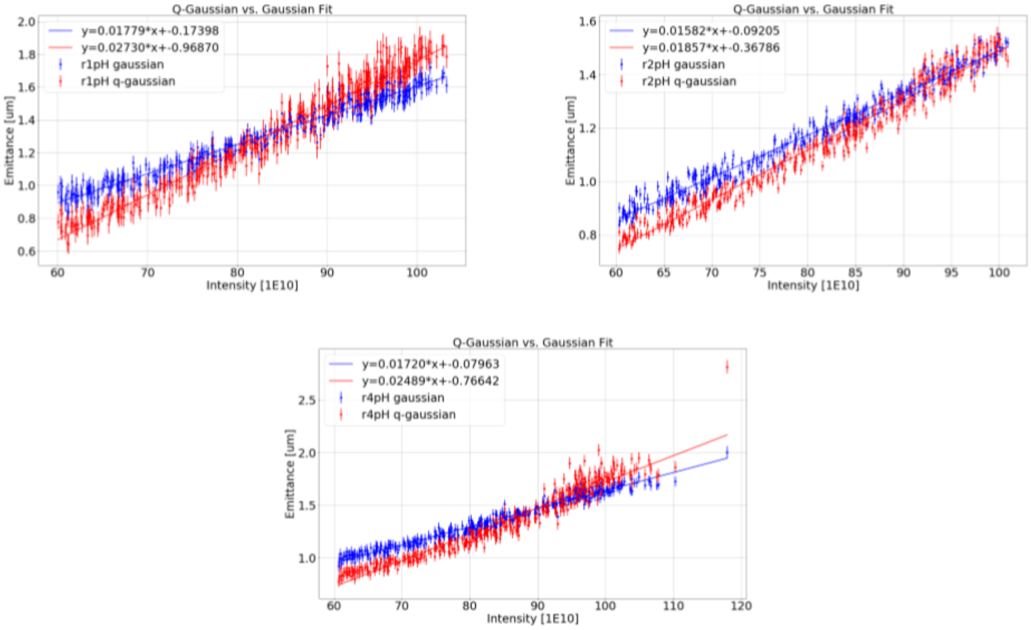

Figure C.2: Impact of the bunch tails for the brightness at the SEM Grids when the beam is extracted from R1, R2 and R4 of the PSB

Bibliography

[1] Oliver Sim Brüning, Paul Collier, P Lebrun, Stephen Myers, Ranko Ostojic, John Poole, and Paul Proudlock. *LHC Design Report Vol.1: The LHC Main Ring.* CERN Yellow Reports: Monographs. CERN, Geneva, 2004.

[2] "CERN Official Website, `https://home.cern/`".

[3] Michael Benedikt, Paul Collier, V Mertens, John Poole, and Karlheinz Schindl. *LHC Design Report Vol.3: The LHC Injector Chain.* CERN Yellow Reports: Monographs. CERN, Geneva, 2004.

[4] K. H. Reich. The CERN Proton Synchrotron Booster. *IEEE Trans. Nucl. Sci.*, 16:959–961, 1969.

[5] M. J. Barnes, L. Ducimetiére, T. Fowler, V. Senaj, and L. Sermeus. Injection and extraction magnets: kicker magnets. 2011.

[6] M. J. Barnes, J. Borburgh, B. Goddard, and M. Hourican. Injection and extraction magnets: septa. 2011.

[7] Federico Roncarolo. *Accuracy of the Transverse Emittance Measurements of the CERN Large Hadron Collider.* PhD thesis, Milan Polytechnic, 2005.

[8] Andrea Santamaría García, Simon Albright, Hannes Bartosik, Jose Briz Monago, Gian Piero Di Giovanni, Vincenzo Forte, Bettina Mikulec, Federico Roncarolo, and Vasilis Vlachoudis. Systematic Studies of Transverse Emittance Measurements Along the CERN PS Booster Cycle. *J. Phys. : Conf. Ser.*, 1067(CERN-ACC-2018-119. 5):TUPAF047. 6 p, 2018.

[9] K. Hanke. Past and present operation of the CERN PS Booster. *Int. J. Mod. Phys.*, A28:1330019, 2013.

[10] Fernandez, Araceli Navarro. Characterization and optimization of CERN Secondary Emission Monitors (SEM) used for beam diagnostics, 2017.

[11] Gilbert Guignard. *Selection of formulae concerning proton storage rings.* CERN Yellow Reports: Monographs. CERN, Geneva, 1977.

[12] Apollinari G., Béjar Alonso I., Brüning O., Fessia P., Lamont M., Rossi L., and Tavian L. *High-Luminosity Large Hadron Collider (HL-LHC): Technical Design Report V. 0.1.* CERN Yellow Reports: Monographs. CERN, Geneva, 2017.

[13] H Damerau, A Funken, R Garoby, S Gilardoni, B Goddard, K Hanke, A Lombardi, D Manglunki, M Meddahi, B Mikulec, G Rumolo, E Shaposhnikova, M Vretenar, and J Coupard. LHC Injectors Upgrade, Technical Design Report, Vol. I: Protons. Technical Report CERN-ACC-2014-0337, Dec 2014.

[14] W Weterings, Masamitsu Aiba, Jan Borburgh, C Carli, T Fowler, and Bethany Goddard. Operational considerations for the psb h- injection system. 09 2009.

[15] L Arnaudon, P Baudrenghien, M Baylac, G Bellodi, Y Body, J Borburgh, P Bourquin, J Broere, O Brunner, L Bruno, C Carli, Friedhelm Caspers, S M Cousineau, Y Cuvet, C De Almeida Martins, T Dobers, T Fowler, R Garoby, F Gerigk, B Goddard, K Hanke, M Hori, M Jones, K Kahle, Willi Kalbreier, T Kroyer, D Küchler, A M Lombardi, L A López-Hernandez, M Magistris, M Martini, S Maury, E Page, M Paoluzzi, M Pasini, U Raich, C Rossi, J P Royer, E Sargsyan, J Serrano, R Scrivens, M Silari, M Timmins, W Venturini-Delsolaro, M Vretenar, R Wegner, W Weterings, and T Zickler. Linac4 Technical Design Report. Technical Report CERN-AB-2006-084. CARE-Note-2006-022-HIPPI, CERN, Geneva, Dec 2006. revised version submitted on 2006-12-14 09:00:40.

[16] G. Rumolo. LIU proton beam parameters. EDMS-1296306/2.

[17] Klaus Wille. *The Physics of Particle Accelerators: An Introduction (First Edition).* Clarendon Press, 2001.

[18] Attila Mate. The Frenet-Serret formulas. Brooklyn College of the City University of New York, Jan 2017. URL: `http://www.sci.brooklyn.cuny.edu/~mate/misc/frenet_serret.pdf`.

[19] Helmut Wiedermann. *Particle Accelerator Physics (Third Edition).* Springer, 2007.

[20] S. Y. Lee. *Accelerator Physics (Third Edition).* Wspc, 2011.

[21] C. Biscari. Transverse Beam Dynamics. African School of Fundamental Physics and Applications 2016. URL: `https://indico.cern.ch/event/528094/contributions/2213316/`.

[22] Andrea Latina. Introduction to Transverse Beam Dynamics. JUAS 2019. URL: `https://indico.cern.ch/event/779575/timetable/`.

[23] Elena Benedetto, Magdalena Anna Cieslak-Kowalska, Vincenzo Forte, and Frank Schmidt. Space charge effects and mitigation in the CERN PS Booster, in view of the upgrade. (CERN-ACC-2016-0108):THPM9X01. 6 p, Aug 2016.

[24] B. J. Holzer. Introduction to longitudinal beam dynamics. 2014.

[25] E. Metral. Longitudinal Dynamics. JUAS 2019. URL: `https://indico.cern.ch/event/779575/timetable/`.

[26] H. Ikeda, J. W. Flanagan, H. Fukuma, S. Hiramatsu, T. Ieiri, H. Koiso, T. Mimashi, and T. Mitsuhashi. Negative momentum compaction at KEKB. *eConf*, C0309101:THWA002, 2003.

[27] Ch Steinbach and M van Rooij. A scanning wire beam profile monitor. *Nuclear Science, IEEE Transactions on*, 32:1920–1922, 11 1985.

[28] G. Sterbini, B. Dehning, S.S. Gilardoni, and A. Guerrero. Beam-based Measurements of the CPS Wire Scanner Precision and Accuracy. In *Proc. 5th International Particle Accelerator Conference (IPAC'14), Dresden, Germany, June 15-20, 2014*, number 5 in International Particle Accelerator Conference, pages 3674–3676, Geneva, Switzerland, July 2014. JACoW. https://doi.org/10.18429/JACoW-IPAC2014-THPME173.

[29] Tilo Strutz. *Data Fitting and Uncertainty.* Springer Vieweq, 2016.

[30] Adrian A. Budini. Extended q-gaussian and q-exponential distributions from gamma random variables. 2015.

[31] S Papadopoulou, F Antoniou, T Argyropoulos, M Fitterer, M Hostettler, and Y Papaphilippou. Modelling and measurements of bunch profiles at the LHC. *Journal of Physics: Conference Series*, 874:012008, jul 2017.

[32] "Q-Gaussian distribution, `https://en.wikipedia.org/wiki/Q-Gaussian_distribution`".

[33] Tirsi Prebibaj, Fanouria Antoniou et al. Brightness Studies - SEM Grids Measurements. LIU-PSB Beam Dynamics WG 16. URL: `https://indico.cern.ch/event/804134/`.

[34] S Hancock and Sanchez Alvarez J-L. A pedestrian guide to online phase space tomography in the CERN complex. Technical Report CERN-PS-RF-NOTE-2001-010, CERN, Geneva, Aug 2001.

[35] Hancock, S. A simple algorithm for longitudinal phase space tomography. Technical Report CERN-PS-RF-NOTE-97-06, CERN, Geneva, May 1997.

[36] S Hancock, P Knaus, and Mats Lindroos. Tomographic measurements of longitudinal phase space density. *Computer Physics Communications*, 121-122, 09 1999.

[37] David Belohrad and Grzegorz Henryk Kasprowicz. Beam intensity measurement system for proton synchrotron booster - art. no. 63470f. *Proceedings of SPIE: Photonics Applications in Astronomy, Communications, Research and High Energy Physics Experiments*, 6347:63470F–1, 10 2006.

[38] G Kasprowicz. Determination of beam intensity and position in a particle accelerator, 2011.

[39] W. Blokland. Beam Current Monitors. USPAS and University of New Mexico. URL: `https://uspas.fnal.gov/materials/09UNM/BeamCurrentMonitors.pdf`.

[40] S. M. Riad. The deconvolution problem: An overview. *Proceedings of the IEEE*, 74(1):82–85, Jan 1986.

[41] Guido Sterbini et al. De-convolution algorithm to properly remove dispersive profile for emittance calculations. LIU-PS Beam Dynamics WG meeting 5. URL: `https://indico.cern.ch/event/676527/`.

[42] G. Sterbini, J.F. Comblin, V. Forte, A. Guerrero, and E. Piselli. Emittance Characterisation of High Brightness Beams in the CERN PS. In *Proc. of International Particle Accelerator Conference (IPAC'16), Busan, Korea, May 8-13, 2016*, number 7 in International Particle Accelerator Conference, pages 299–302, Geneva, Switzerland, June 2016. JACoW. doi:10.18429/JACoW-IPAC2016-MOPMR028.

[43] H. Braun. Emittance Diagnostics I, II. CERN Accelerator School, Dourdan 2008. URL: `https://cas.web.cern.ch/schools/dourdan-2008`.

[44] H Bartosik and G Rumolo. Beams from the injectors. pages 233–238. 6 p, 2017.

[45] H. Bartosik. Injectors beam performance evolution during run 2. in *Proc. of the 8th LHC Operations Evian workshop (EVIAN'19)*, Evian, France, Feb. 2019.

[46] Fanouria Antoniou et al. PSB. ABP Injectors Day. URL: `https://indico.cern.ch/event/799216/`.

[47] G.P. Di Giovanni et al. Comparison of Different Transverse Emittance Measurement Techniques in the Proton Synchrotron Booster. In *Proc. 9th International Particle Accelerator Conference (IPAC'18), Vancouver, BC, Canada, April 29-May 4, 2018*, number 9 in International Particle Accelerator Conference, pages 232–235, Geneva, Switzerland, June 2018. JACoW Publishing. https://doi.org/10.18429/JACoW-IPAC2018-MOPMF054.

[48] Fanouria Antoniou et al. Brightness and transverse emittance from the PSB. LHC Injectors Upgrade Workshop. URL: `https://indico.cern.ch/event/774181/timetable/#20190213.detailed`.

[49] G.P. Di Giovanni et al. PSB WS vs SEM-grids emittance measurements. LIU-PS Beam Dynamics WG meeting 5. URL: `https://indico.cern.ch/event/676527/`.

[50] P.K. Skowroński, M. Giovannozzi, and A. Huschauer. Linear and Non-Linear Optics Measurements in PS using Turn-by-Turn BPM Data. In *Proc.*

10th International Partile Accelerator Conference (IPAC'19), Melbourne, Australia, 19-24 May 2019, number 10 in International Partile Accelerator Conference, pages 1114–1117, Geneva, Switzerland, Jun. 2019. JACoW Publishing. https://doi.org/10.18429/JACoW-IPAC2019-MOPTS102.

[51] J. Keintzel et al. Second Order Dispersion Measurements in LHC. In *Proc. 10th International Partile Accelerator Conference (IPAC'19), Melbourne, Australia, 19-24 May 2019*, number 10 in International Partile Accelerator Conference, pages 496–499, Geneva, Switzerland, Jun. 2019. JACoW Publishing. https://doi.org/10.18429/JACoW-IPAC2019-MOPMP027.

[52] Peter Forck, P Kowina, and Dmitry Liakin. Beam position monitors. *Synchrotron Radiation News*, 1, 01 2008.

[53] "MAD - Methodical Accelerator Design, `http://mad.web.cern.ch/mad/`".

[54] A. Garcia-Tabares, P.K. Skowroński, and R. Tomás. Optics Measurements in the CERN PS Booster Using Turn-by-Turn BPM Data. In *Proc. 10th International Partile Accelerator Conference (IPAC'19), Melbourne, Australia, 19-24 May 2019*, number 10 in International Partile Accelerator Conference, pages 285–288, Geneva, Switzerland, Jun. 2019. JACoW Publishing. https://doi.org/10.18429/JACoW-IPAC2019-MOPGW080.

[55] A Wegscheider, Andy Langner, Rogelio Tomas, and Franchi Andrea. Analytical n beam position monitor method. *Physical Review Accelerators and Beams*, 20, 11 2017.

[56] Ana Garcia-Tabares, Felix Carlier, Jaime Maria Coello de Portugal, Andy Langner, Ewen Maclean, Lukas Malina, Tobias Persson, Piotr Skowroński, Matteo Solfaroli Camillocci, and Rogelio Tomás. Optics-measurement-based BPM Calibration. (CERN-ACC-2016-188):THPMB041. 4 p, 2016.

[57] F. Antoniou et al. Transverse Emittance Studies at Extraction of the CERN PS Booster. In *Proc. 10th International Partile Accelerator Conference (IPAC'19), Melbourne, Australia, 19-24 May 2019*, number 10 in International Partile Accelerator Conference, pages 1058–1061, Geneva, Switzerland, Jun. 2019. JACoW Publishing. https://doi.org/10.18429/JACoW-IPAC2019-MOPTS087.

[58] A Jansson, M Lindroos, M Martini, and Karlheinz Schindl. Study of emittance blow-up sources between the PS booster and the 26 GeV PS. (CERN-PS-98-058-OP):4 p, Nov 1998.

[59] M. Fraser. Transverse effects with twice brightener beams in the PS. LIU workshop, Montreux, 2019.

[60] Vincenzo Forte, Simon Albright, Wolfgang Bartmann, Gian Piero Di Giovanni, Matthew Fraser, Christoph Heßler, Alexander Huschauer, and Adrian Oeftiger.

Overview of the CERN PSB-to-PS Transfer Line Optics Matching Studies in View of the LHC Injectors Upgrade Project. page WEP2PO006. 6 p, 2018.

[61] A. G. Barnston. Correspondence among the Correlation, RMSE, and Heidke Forecast Verification Measures; Refinement of the Heidke Score. *Weather and Forecasting*, 7:699–700, December 1992.

[62] Tirsi Prebibaj, Fanouria Antoniou et al. Emittance Reconstruction Algorithms. LIU-PSB Beam Dynamics WG 19. URL: `https://indico.cern.ch/event/832290/`.

[63] Tirsi Prebibaj, Fanouria Antoniou et al. Transverse Emittance Measurements. LIU-PSB Beam Dynamics WG 12. URL: `https://indico.cern.ch/event/759235/`.

[64] Tirsi Prebibaj, Fanouria Antoniou et al. Emittance measurements analysis in the PSB. ABP Group Information Meeting. URL: `https://indico.cern.ch/event/819845/`.

[65] Eugenio Senes, Jonathan Emery, M Fraser, A Ollacarizqueta, A Huschauer, Federico Roncarolo, Jose Luis Sirvent Blasco, P. Sk, Frank Tecker, and V Forte. Transverse emittance measurement in the cern proton synchrotron in view of beam production for the high-luminosity lhc. 05 2019.